Effects of lightning on UAM aircraft: complex zoning and direct effects on composite prop-rotor blade

Y. G. Kim[a, b], J. H. Jo[a], D. H. Kim[a], H. Lee[a], R. S. Myong[a,*]

[a]School of Mechanical and Aerospace Engineering and Research Center for Aircraft Core Technology, Gyeongsang National University, 501 Jinjudaero, Jinju, Gyeongnam 52828, South Korea

[b]Aerospace EM Technology Center, Korea Testing Laboratory, 10 Chungui-ro, Jinju, Gyeongnam 52852, South Korea.

[*]Corresponding author: E-mail address *myong@gnu.ac.kr* (R.S. Myong)

Abstract

A UAM is a small to medium-distance air transportation system that carries passengers in and out of the city by flying at low altitudes. UAMs are based on eco-friendly electric propulsive systems to enhance mobility and maximize the use of three-dimensional airspace. However, UAM aircraft are very vulnerable to lightning strikes due to their relatively small size and flight characteristics, flying close to the ground. To tackle this problem, the present study developed a lightning zoning method for UAM aircraft with complex configurations and investigated the direct effects of lightning strikes on the prop-rotor blade of a UAM aircraft. First, computational simulation models for zoning analysis were developed for four representative UAM aircraft (one wingless multi-copter, one winged lift/cruise, and two winged vectored thrust types). The lightning zoning analysis identified the prop-rotor blade tips as Zone 1A, which has a high probability of initial lightning attachment. The direct effects of lightning strikes on a prop-rotor blade made of woven carbon/epoxy laminate were then investigated using both experimental and numerical methods. In general, the damage pattern of the simulation results agreed fairly well with the damage pattern in the experimental results. Moreover, it was shown that the prop-rotor blade of a relatively small UAM aircraft can suffer more damage, even after being struck by the lightning of the same intensity. In the future, since batteries, electric motors, inverters, and hydrogen fuel tanks, which are required by the new propulsion systems in UAM aircraft, will be increasingly used, designing a lightning protection system that properly reflects these changes will emerge as an important issue.

Keywords: Urban air mobility (UAM) aircraft; lightning zoning; lightning direct effects; prop-rotor blade; lightning test; multi-physics simulation

1. Introduction

Countries around the world are encountering serious problems with traffic congestion and environmental pollution due to the increase in the number of cars in urban areas. As a solution to address these problems, new means of transportation based on enhanced mobility and eco-friendly propulsive systems are increasingly being studied. For instance, many companies around the world are attempting to develop urban air mobility (UAM) aircraft which can take maximum advantage of three-dimensional airspace [1-6]. A UAM is a small to medium-distance air transportation system that flies passengers into and out of the city at low altitude. Depending on the presence or absence of wings and the type of lift and propulsion system, UAM aircraft can be classified into three types: wingless multi-copter, winged lift and cruise, and winged vectored thrust [7], as summarized in Table 1. The vector thrust type, which uses a double tilt rotor, is known to be highly efficient.

Among various weather-related safety factors (external air disturbance, lightning, icing [8-11], etc.), UAM aircraft are very vulnerable to lightning strikes due to their relatively small size and flight characteristics, that is, flying close to the ground. Furthermore, lightning strikes, which may directly be visible to the eyes of passengers aboard a UAM aircraft with a large windshield, can have a highly negative impact on the public's acceptance of the safety of UAM aircraft.

Because of their unique overall configuration and complex propulsion systems, UAM aircraft have different lightning characteristics, in lightning zoning and sweeping, compared to conventional aircraft. This requires reconsideration of the basic concept of lightning effects on UAM aircraft.

The characteristics of UAM aircraft and associated lightning effects are summarized in Fig. 1. UAM aircraft being designed for future urban transport mostly have a flight envelope with low altitude and low speed. The vulnerability of UAM aircraft to lightning can be divided into two categories: the probability of being struck and the severity of the damage after being struck. Compared to conventional aircraft, UAM aircraft are expected to have a higher probability of being struck in two aspects. First, increased pollution and dense structures in urban areas will increase the frequency of lightning strikes, including the indirect effects of lightning strikes by adjacent UAM aircraft or buildings. Second, UAM aircraft flying at low altitudes (0.5-1.5 km) will experience a high frequency of lightning strikes because they are more likely to be exposed to the cloud-to-ground (CG) lightning strike environment (taking up about 40%), which is a high proportion of the three types of lightning discharge [12-16]. In addition, because the dwell time of the swept lightning stroke increases due to low flight speed (100~200km/h, significantly lower than that of conventional aircraft), there is a high possibility that the frequency of lightning strikes may increase [17-22]. Moreover, the severity of damage after being struck by lightning will be higher compared to conventional aircraft. The reason is that the magnitude of damage at the lightning attachment site is similar, but will cause greater damage to UAM aircraft, which are relatively small compared to conventional aircraft. However, this prediction will have to be confirmed by collecting lightning strike data through actual UAM aircraft operations in urban areas in the future.

Lightning strikes can generate high-temperature heat and strong magnetic fields, resulting in damage to aircraft structures and interference with navigation systems. In addition, the increasing use of composites to reduce weight, more electrification of the propulsion system to reduce noise, and more integration and digitization of electronic equipment to make them compact and multi-functional, all make UAM aircraft more vulnerable to lightning strikes [23, 24]. Moreover, since UAM aircraft windshields often occupy a large portion of the fuselage, they suffer from low electro-magnetic shielding capability, because the material of the windshield has low magnetic permeability [25-27]. Consequently, lightning strikes are the most lethal threat to the safe operation of UAM aircraft [28-32].

When UAM aircraft operate in urban areas, cloud-to-ground lightning activity is increased by the urban effect [33-37]. The urban effect is mainly caused by thermal phenomena due to the urban heat islands (UHI) and an increase in pollution concentration due to concentrated human activities [38-40]. Increased lightning frequency is closely linked to pollution, which enhances the development of thunderclouds [41]. Three lightning strike scenarios for UAM aircraft operating in urban environments with increased lightning activity can be identified, as illustrated in Fig. 2.

The first case is when lightning strikes a UAM aircraft directly. The second case is when a UAM aircraft is indirectly affected by lightning strikes on other UAM aircraft flying at close range. Lastly, there is a case when a nearby high-rise building is struck by lightning, affecting adjacent UAM aircraft in flight. These lightning strikes may induce electromagnetic interference (EMI), electromagnetic pulse (EMP), and flash effects on UAM aircraft flying nearby. In addition, because UAM aircraft operate near the city center, critical lightning strikes have the potential to lead to serious accidents due to the difficulty in using emergency avoidance landing procedures. Therefore, airworthiness certification is required for UAM aircraft, since they are manned transportation vehicles for people to board [42].

As more UAM aircraft begin to operate in urban airspace, they will become more vulnerable to lightning strikes [43, 44]. The effects of lightning strikes on aircraft can be classified into direct and indirect effects. The direct effects of lightning strikes include physical damage such as melting, drilling, vaporization and combustion to the skin or structure outside the aircraft, as well as arcs occurring at the joints of airframe structures, and fuel ignition [45, 46]. The indirect effects of lightning include the failure or damage of electrical equipment caused by strong induced currents generated in the aircraft structure, electrical circuits, and components by the electromagnetic field formed during lightning strikes [47].

Table 1 Classification of UAM aircraft by lift and propulsion system.

Item	**Wingless**	**Winged**	
Type	Multi-copter	Lift+cruise	Vectored thrust
	 	 	 
Efficiency	Low	Mid	High
Major companies	VOLOCOPTER, EHANG	BOEING, JOBY, CORA	AIRBUS, LILIUM, HYUNDAI, BELL

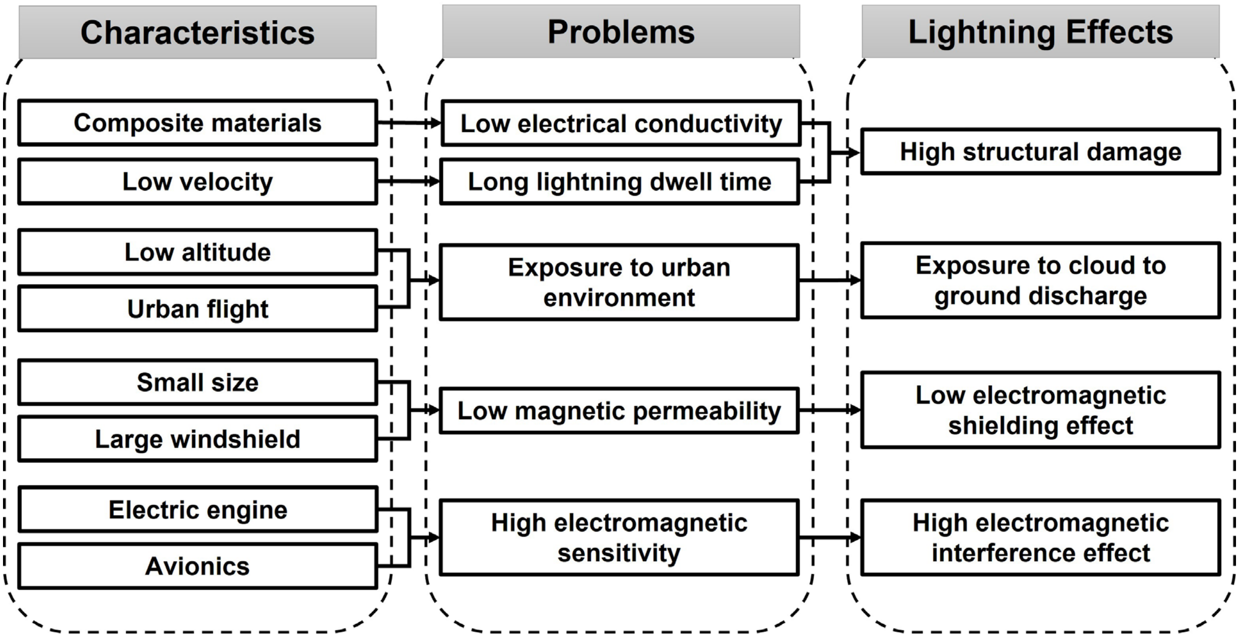

Fig. 1. Characteristics of UAM aircraft and associated lightning effects.

Fig. 2. Effects of urban lightning activity on UAM aircraft: (a) direct lightning strike on UAM aircraft; (b) lightning strike on adjacent UAM aircraft; (c) lightning strike on nearby tall building.

To the best of our knowledge, no experimental studies have been conducted on the direct effects of lightning strikes on UAM aircraft in flight. However, there has been an experimental study of the moment when a much smaller drone similar to a UAM aircraft was struck by lightning while hovering inside the laboratory, as reproduced in Fig. 3 [48]. The lightning strike hit the drone's motor propeller cap and then escaped through the landing gear. Interestingly, the drone's battery was not damaged in this laboratory test. This may be because the battery was covered by a metal case that acted like a Faraday cage. However, the propeller was detached from the motor and flew away, causing the drone to crash. From this observation, a serious threat of lightning strikes to the lift and propulsion system of UAM aircraft can be inferred.

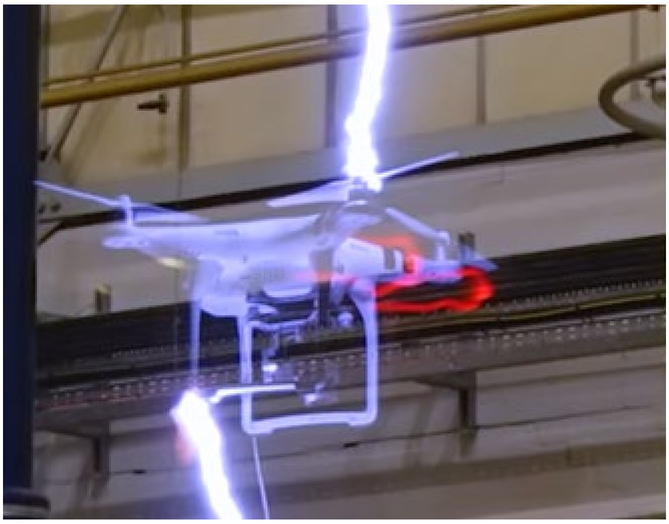

Fig. 3. The moment when a small drone is struck by lightning while hovering [48].

Lightning zoning for aircraft is a method of classifying lightning strikes by zones that take various forms depending on the initial attachment point of the lightning strike. Aircraft have different probabilities of lightning attachment depending on the configuration and surface conditions of the aircraft. An aerospace recommendation, SAE ARP 5414B, defines the lightning strike area for each aircraft configuration, and identifies areas with high probability of initial lightning strikes [49, 50]. Since the electric field is concentrated at a point where the radius of curvature is small, or the three-dimensional shape changes rapidly, lightning strikes are highly likely to be attached to the nose, wing tip, blade tip, engine inlet lip, and landing gear of the aircraft [51-58]. Lightning zoning can be classified into several zones: 1A, 1B, 1C, 2A, 2B, and C, as specified in SAE ARP 5414B.

The overall configuration of the aircraft is the biggest factor defining lightning zoning for aircraft. However, the current certification guidelines developed for conventional aircraft do not provide clear guidelines for lightning zoning for UAM aircraft which have drastically different configurations, such as multi-copters. Therefore, new lightning zoning for UAM aircraft needs to be established which considers their unique configuration and flight characteristics (flight speed and altitude).

In addition to the overall configuration, the prop-rotor blade of a UAM aircraft is another major factor that is significantly different from existing aircraft in terms of lightning effects [59-66]. The prop-rotor blade used in UAM aircraft is considerably smaller than the rotor blade of a conventional rotorcraft [67-77], so it can suffer relatively more damage from lightning strikes of the same intensity. These prop-rotor blades are mainly made of carbon fiber reinforced plastic (CFRP) composites with excellent mechanical strength and chemical stability and light weight [23, 78-86]. However, since the degree of physical damage caused by lightning is greatly affected by the surface current distribution over the outer skin, CFRP structures with low electrical conductivity are more vulnerable to lightning than metals. The high electrical resistance of CFRP absorbs more electrical energy, which is instantaneously converted into thermal energy (Joule heating). This prevents the fast conduction of lightning currents, resulting in arc sparks, Joule heating, generation of magnetic forces or dielectric breakdown [87-89]. In addition, the resin matrix constituting CFRP has low thermal stability, and deteriorates, cracks, or burns due to Joule heating or sparks caused by lightning strikes [90, 91]. Therefore, since composite materials are increasingly used in UAM aircraft, it becomes very important to analyze the effects of lightning strike and develop a high-efficiency lightning protection system [92-98].

The goal of this work is two-fold: presenting a lightning zoning method for UAM aircraft with complex configurations and investigating the direct effects of lightning strikes on the prop-rotor blade of UAM aircraft using both experimental and numerical methods. *To the best of the author's knowledge, there have been no previous studies of the effects of lightning on UAM aircraft*.

First, we consider four representative UAM aircraft (one wingless multi-copter, one winged lift/cruise, and two winged vectored thrust types), and then develop a computational simulation model for the zoning analysis of each aircraft. Then, by applying a partial differential equation-based electromagnetic numerical simulation, lightning zoning is calculated for UAM aircraft with very complex configurations. The lightning zoning differs depending on the shape and surface condition of the UAM aircraft, resulting in different lightning protection coverage.

Next, a specimen unit test was performed on the prop-rotor blade identified as Zone 1A, and quantitative data on the degree of damage for a given lightning [99, 100] were obtained. In parallel, an electrical-thermal coupling numerical simulation considering the change in arc channel expansion with time [101-111] was applied to the woven carbon/epoxy laminate, to predict the degree of damage caused by a lightning strike to the composite prop-rotor blade. Finally, by comparing the numerical simulation results of the rotor blades of the rotorcraft and the prop-rotor blades of the UAM aircraft, the damaged area was quantitatively evaluated based on the length of the chord.

2. Lightning zoning for UAM aircraft

2.1. Lightning mechanism of UAM Aircraft

In general, lightning strikes occurring at an altitude higher than 4.5 km are likely to be in-cloud discharges between the positive and negative charges in a cloud. On the other hand, below 4.5km, there is a high possibility of cloud-to-ground lightning strikes [14-16]. UAM aircraft that operate at an altitude much lower than 4.5km, between the thundercloud and the ground, are highly likely to be struck by cloud-to-ground lightning strikes. Cloud-to-ground lightning strikes can be classified into four types, as shown in Fig. 4 [112]. In general, downward negative lightning (type (a) shown in Fig. 4) occurs on flat terrain with moderately high objects (less than 100m from the ground) and account for 90 percent or more of the global cloud-to-ground lightning strikes. The remaining 10 percent or less are attributed to downward positive lightning (type (c)). Upward lightning strikes (type (b) and type (d)) generally occur only in the presence of objects higher than about 100 m.

Lightning strikes on UAM aircraft occur when a stepped leader generated by a cloud-to-ground lightning strike approaches the aircraft. At this moment, as shown in Fig. 5, due to the corona phenomenon, a streamer is generated in the aircraft, and the stepped leader and streamer meet to create a path of lightning. The electric energy of the lightning enters the aircraft along the generated path, moves to the outside of the aircraft along the wires of structures or electronic equipment inside the aircraft, and is released toward the ground.

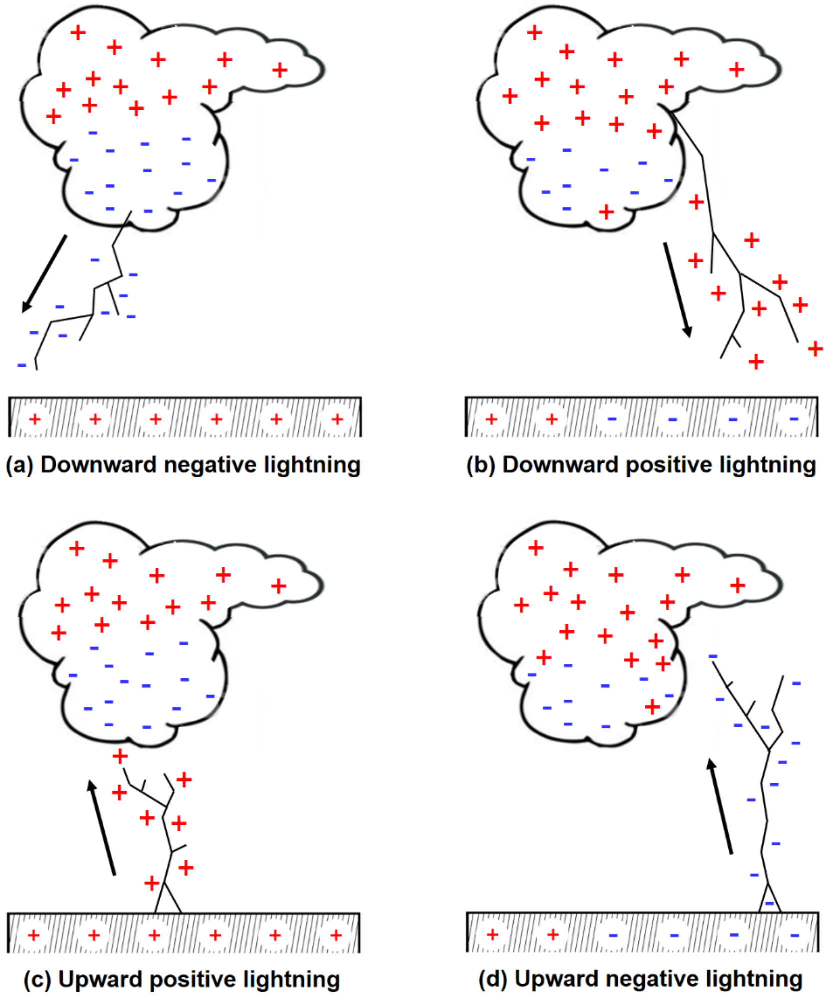

Fig. 4. Schematic of four types of cloud-to-ground lightning.

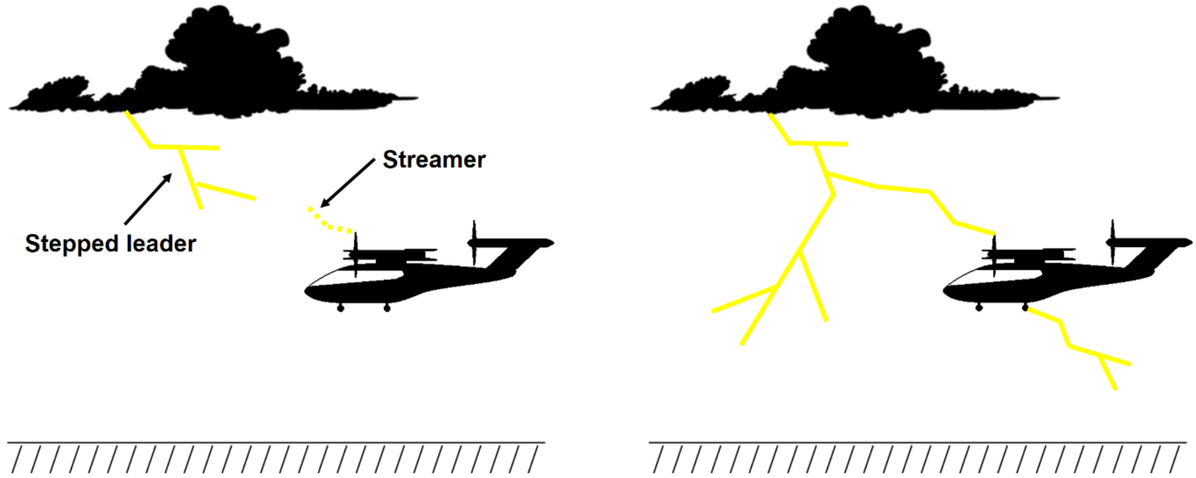

Fig. 5. Mechanism of a cloud-to-ground type lightning strike on UAM aircraft.

2.2. Zoning analysis method and boundary condition

Many previous studies have been conducted to predict the initial attachment area of a lightning strike on aircraft [51-58]. However, most of the previous methods have limitations when it comes to predicting lightning zoning for UAM aircraft which have drastically different configurations, such as multi-copters. An aerospace recommendation, SAE ARP 5414B, describes the lightning zoning by aircraft size, propulsion type, and fixed and rotary wing aircraft. SAE ARP 5414B basically defines a lightning zoning based on available data from lightning strikes on actual aircraft. It is difficult to apply the method described in SAE ARP 5414B to UAM aircraft because the recently developed UAM aircraft have very diverse configurations due to their complex lift and propulsion systems, and the lack of lightning strike data.

The rolling sphere method is a method for determining a lightning strike zone by drawing a circle tangent to the aircraft surface. This method has the advantage of being simple and intuitively applicable without relying on a complicated procedure. However, this method is also difficult to apply to UAM aircraft because it is not clear how to determine the radius of the rolling sphere for a UAM aircraft with a configuration that is drastically different from that of a conventional aircraft [57]. The ONERA code developed in France is a method of probabilistically predicting the lightning attachment area [52, 53]. However, this code so far has not yet been applied to the lightning zoning for UAM aircraft with various configurations.

In this study, in order to predict the lightning zoning of the UAM aircraft, a complex electrostatic field analysis was performed using the EM model of CST, a commercial S/W [58].

Among the laws constituting the Maxwell equation, Gauss' law describes the magnitude of the electric field generated by electric charges. The equation can be expressed as follows [113-115],

$$\nabla \cdot \mathbf{D} = \rho_v, \tag{1}$$

where $\mathbf{D}$ is the electric displacement field in units of C/m^2, and ρ_v is the free charge density in units of C/m^3. The relationship between the electric displacement field and the electric field and the relationship between the electric potential gradient and electric field can be expressed as follows,

$$\mathbf{D} = \varepsilon \mathbf{E},\ \mathbf{E} = -\nabla V, \tag{2}$$

where $\mathbf{E}$ is the electric field in units of V/m, ε is the electric permittivity, and V is the electric potential in units of V. By substituting equation (2) into equation (1), the following Poisson's partial differential equation of the electrostatic field can be obtained,

$$-\nabla \cdot (\varepsilon \nabla V) = \rho_v. \tag{3}$$

For homogeneous media, this Poisson's equation is reduced to

$$\nabla^2 V = -\frac{\rho_v}{\varepsilon}. \tag{4}$$

Based on the finite element method (FEM) technique, the EM model obtains a solution by dividing a computational domain into a finite number of elements and approximating it with a set of equations [116]. The free charge density distribution of the UAM aircraft is then calculated from the potential difference with the surroundings according to the flight environment. In this distribution, the area where the strength of the electrostatic field is high is defined as the initial attachment area of the lightning strike.

Electrostatic potential simulations of UAM aircraft in flight were performed for two cases: exposure to the downward ground discharge environment, and flying in the open air, as shown in Fig. 6 [58, 117-119]. In the boundary value problem (BVP) approach, fixed potentials are assigned to two boundaries, and the electrostatic field distribution is predicted based on potential information about the aircraft's surface. UAM aircraft operating at low altitudes are mainly placed in a downward ground discharge environment, which can be implemented by dividing the upper region (thundercloud, high voltage) and lower region (ground, low voltage), as shown in Fig. 7 (a). On the other hand, in the initial value problem (IVP) approach, the fixed potential is distributed over the surface of the aircraft, which can reduce the computing time. Using this approach, it is possible to realize the operating environment of an aircraft flying in an open air space, as shown in Fig. 7 (b). This approach focuses on predicting the initial lightning attachment area from the distribution of the static electric field after applying the fixed potential to the aircraft. In this calculation, the skin material of the UAM aircraft was assumed to be a perfect electric conductor.

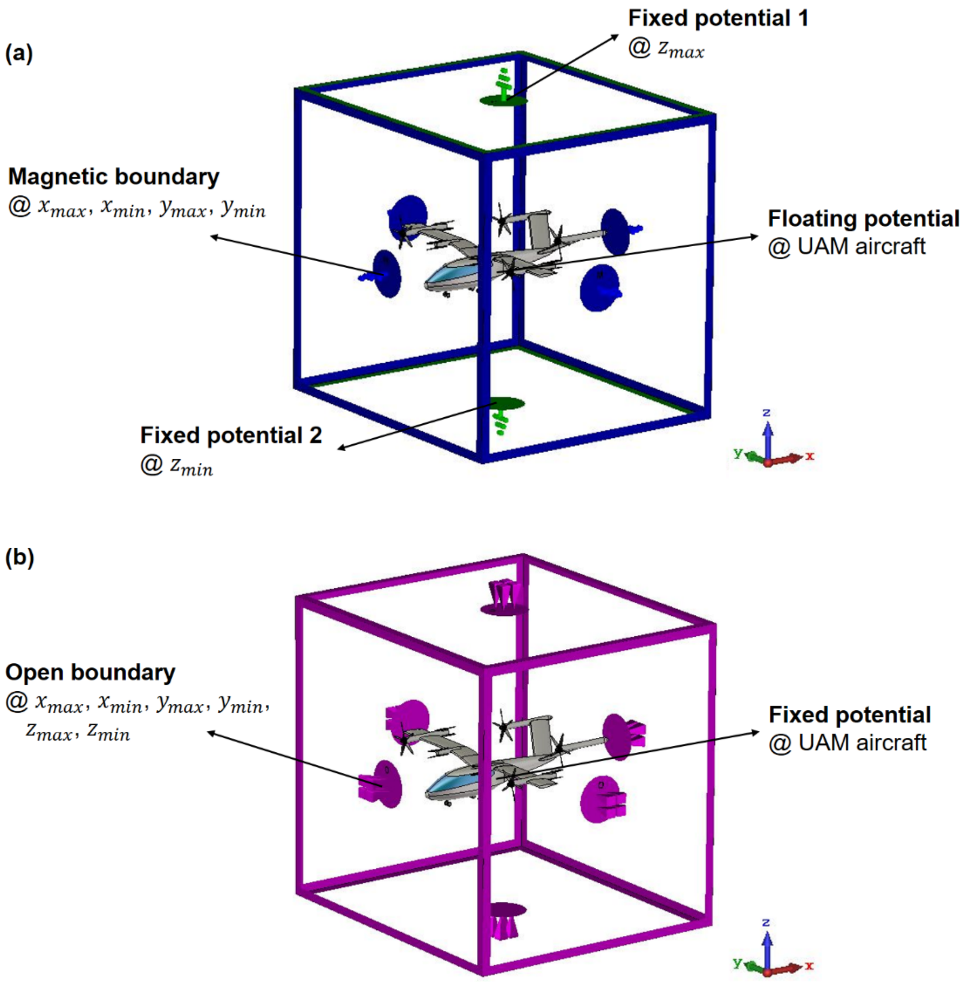

Fig. 6. Boundary conditions: (a) BVP case; (b) IVP case.

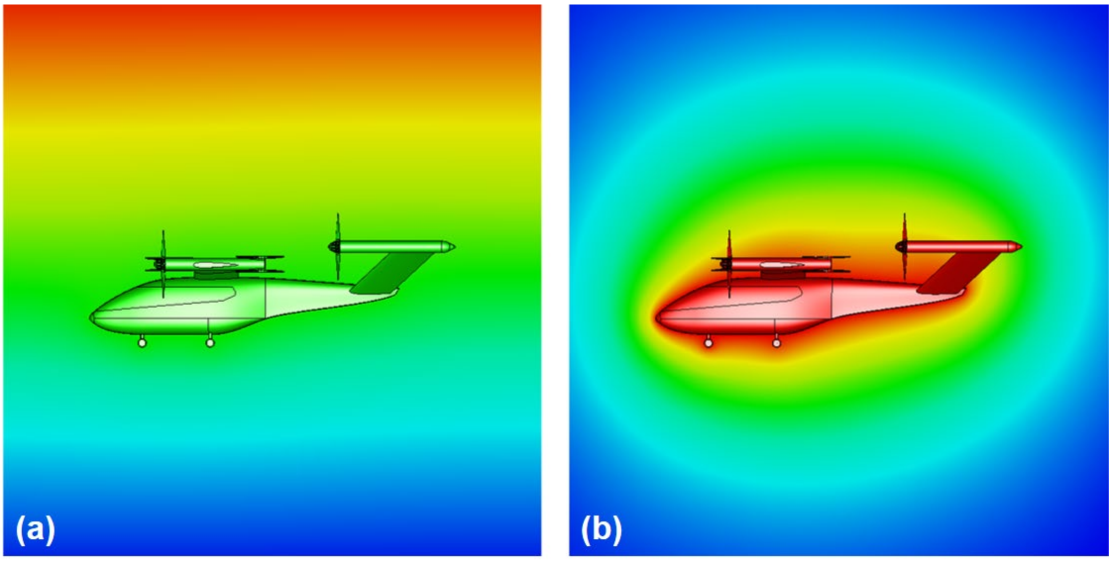

Fig. 7. Electric potential distribution: (a) BVP case; (b) IVP case.

2.3. Validation of the lightning zoning simulation

In order to verify the effectiveness of the new lightning zoning simulation technique, the EC-155B model, a civilian rotorcraft manufactured by AIRBUS Helicopter, was considered. SAE ARP 5414B specifies the lightning zoning for rotorcraft as illustrated in Figure 8 [49]. The electrostatic potential simulation results obtained by applying the BVP and IVP approaches to the EC-155B model were compared with SAE ARP 5414B.

Figures 9 and 10 show that the probability of a lightning zoning is high in the area where the electrostatic field is concentrated due to the small radius of curvature and the rapid change in the three-dimensional shape. Also, some differences between the two approaches can be found with the static potential distribution on the nose part of the rotorcraft fuselage, the lower surface of the blade, and the end plate of the horizontal stabilizer.

To validate the present numerical solutions of the Poisson's partial differential equation of the electrostatic field, the detailed comparison of lightning zones specified in SAE ARP 5414B (based on actual rotorcraft lightning strike data) and obtained by the present method on the EC-155B rotorcraft model is presented in Fig. 11. It was found that Zones 1B, 2A, and 3 are almost identical, confirming the validity of the current method. In addition, the lightning attachment area of the integrated tail rotor, which is a characteristic of EC-155B, also showed a similar trend. Furthermore, the region of Zone 3, where the probability of lightning initial attachment is low, was predicted to be the region with low electrostatic field in the present simulation.

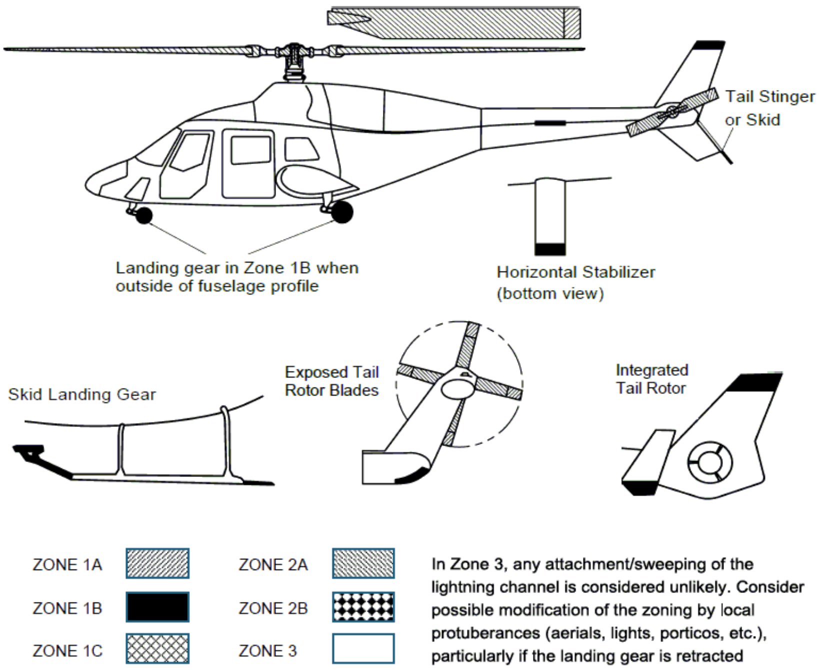

Fig. 8. Example of lightning zones for rotorcraft [49].

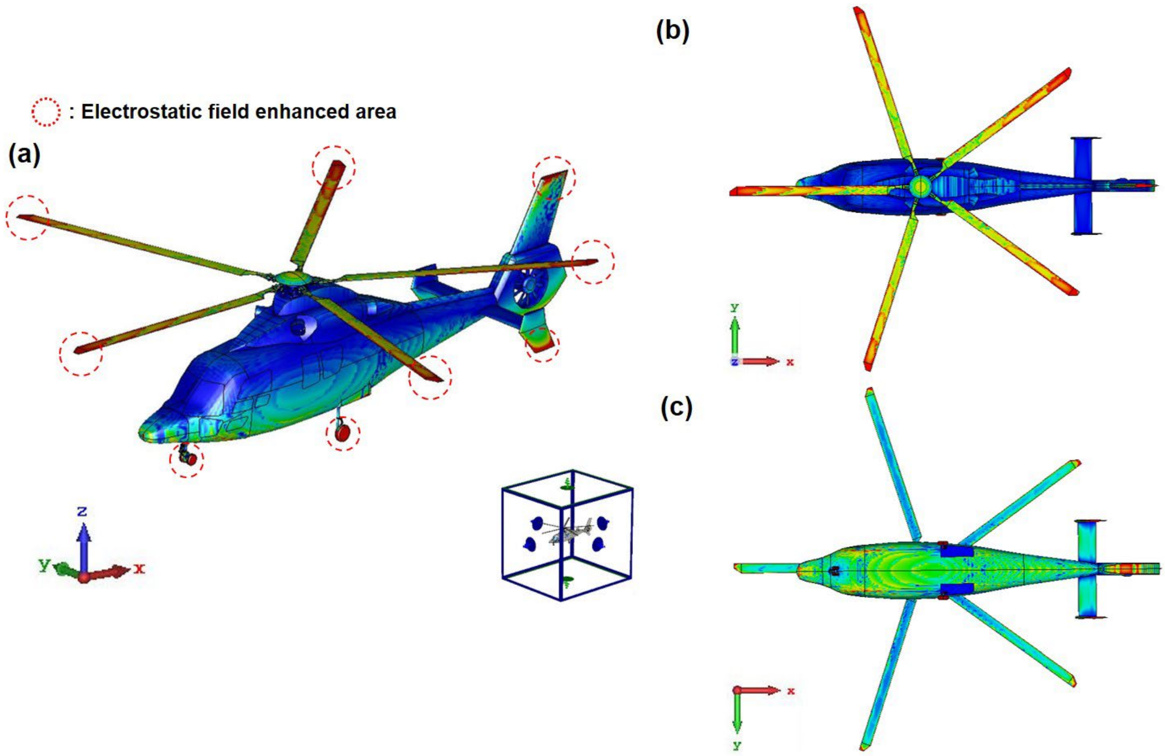

Fig. 9. Electrostatic field distribution of EC-155B (BVP): (a) perspective; (b) top view; (c) bottom view.

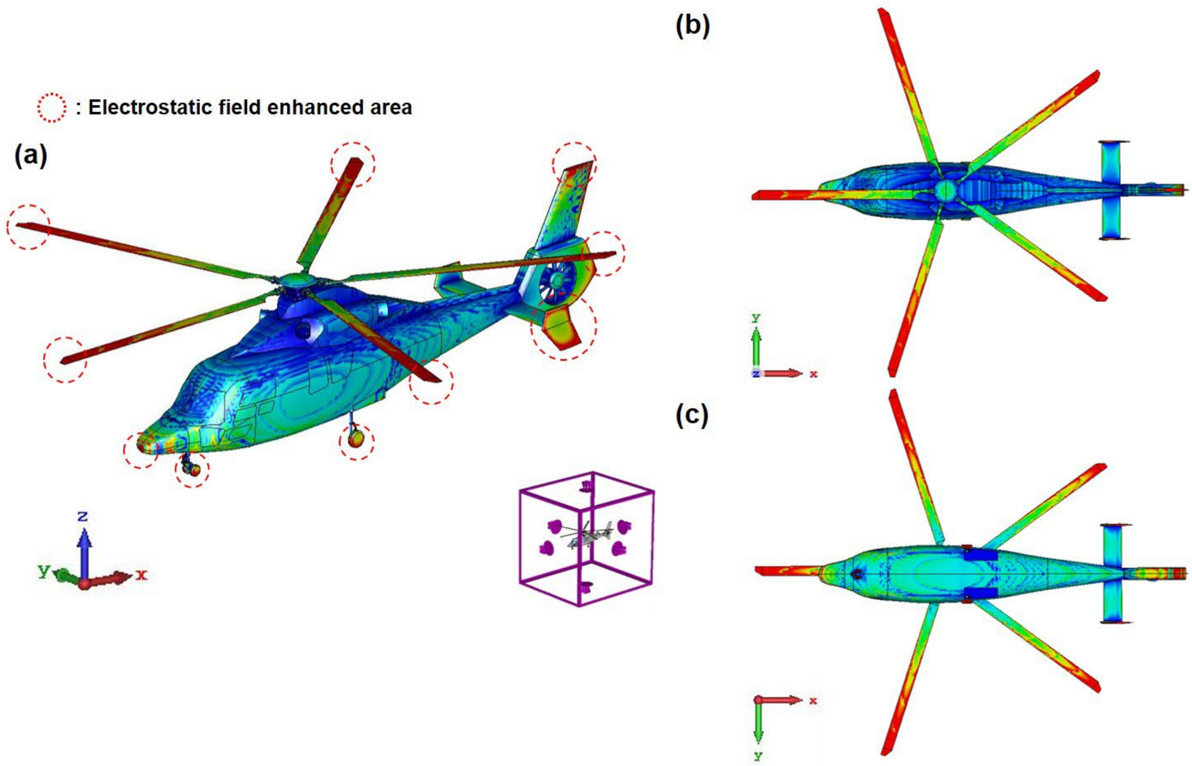

Fig. 10. Electrostatic field distribution of EC-155B (IVP): (a) perspective; (b) top view; (c) bottom view.

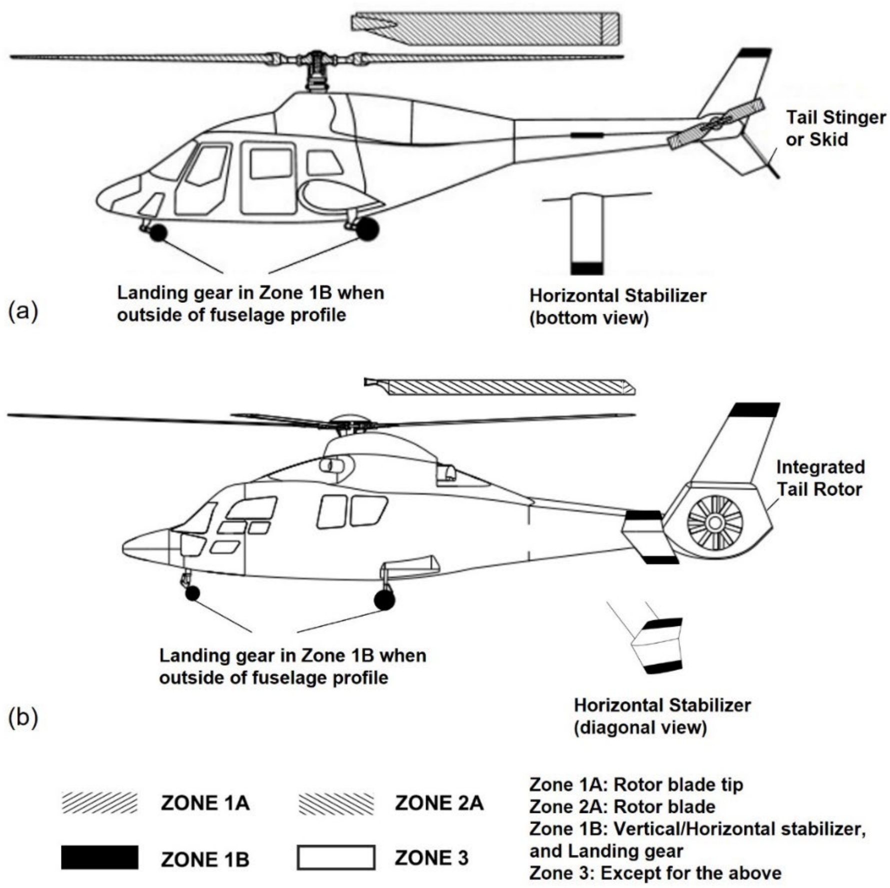

Fig. 11. Comparison of lightning zones for rotorcraft: (a) SAE ARP 5414B; (b) present result.

2.4. Lightning zoning for the UAM aircraft

In this section, lightning zoning for a UAM aircraft with diverse configurations was investigated, using the electrostatic potential simulation. Using the distribution of the electrostatic field of the UAM aircraft, it is necessary to identify the initial lightning attachment area and the area where the lightning protection system is located. Because UAM aircraft fly at much slower speeds than conventional aircraft, sweep stroke phenomena may not be significant, and therefore attachment points at leading edges, frontal surfaces or any lower extremities may all receive components of the flash.

A total of four UAM aircraft were considered: a Volocopter 2X with multi-copter [84], Pegasus with lift-cruise type propulsion [20], S-A1 with a vectored thrust type propulsion [86], and a Nexus 4EX with a ducted vectored thrust type propulsion [20]. The main specifications of the four configurations are summarized in Tables 2 and 3. The geometry used for computational analysis was modeled using CATIA's generative shape design.

Figures 12 and 13 show the electrostatic potential simulation results of the Volocopter 2X with multi-copter obtained with the BVP and IVP approaches, respectively. With the BVP approach, the initial lightning attachment area was distributed over the entire area including the tip of all prop-rotor blades at the top, and the tip and center of the landing skid at the bottom. On the other hand, with the IVP approach, the initial lightning attachment area was mainly formed in the middle of the structure connecting the prop-rotor blade tip, located outside the upper part and the outermost prop-rotor. In addition, it was found that a weak initial lightning attachment area was formed at the end of the lower landing skid.

Figures 14 and 15 show the electrostatic potential simulation results of the Pegasus with lift-cruise type propulsion obtained with the BVP and IVP approaches, respectively. In the BVP approach, the initial lightning attachment area was formed at the tip of the wing, the upper part of the fuselage, and the tip of the thrust rotor blade. In addition, the entire lower surface of the landing skid located at the bottom was identified as the initial lightning attachment area. With the IVP approach, unlike the BVP approach, the initial lightning attachment area was formed at the tip of each prop-rotor blade, as well as the tip of the upper wing. In particular, the initial lightning attachment area was strongly formed on the outermost four prop-rotor blades among the eight prop-rotor blades located at the top. Also, unlike the BVP approach, the initial lightning attachment area was formed only at the end of the lower landing skid, not the entire area.

Figures 16 and 17 show the electrostatic potential simulation results of the S-A1 with vectored thrust type propulsion obtained with the BVP and IVP approaches, respectively. With the BVP approach, the initial lightning attachment area was distributed to the tip of each prop-rotor blade and the lower landing gear. In contrast, in the IVP approach, the initial lightning attachment area was formed at the nose part of the fuselage, including the tips of all the prop-rotor blades and the tip of the wing. An initial lightning attachment area did not form in the lower landing gear.

Lastly, Figs. 18 and 19 show the electrostatic potential simulation results of the Nexus 4EX with ducted vectored thrust type propulsion obtained with the BVP and IVP approaches, respectively. With the BVP approach, the initial lightning attachment area formed at the top of the duct surrounding the prop-rotor blade of the Nexus 4EX model, and at the tip of the vertical tail. An initial lightning attachment area was also formed in the lower landing gear. With the IVP approach, similar to the BVP approach, the initial lightning attachment area formed at the upper part of the duct, the tip of the vertical tail, and the landing gear, as well as at the nose, wing tips, and the front of the duct.

Lightning strikes on prop-rotor blades can fatally affect the safe operation of UAM aircraft. The results of the multi-copter type Volocopter 2X and the vectored thrust type S-A1 confirmed that the initial lightning attachment area was formed at the tip of a number of prop-rotor blades in both cases. This means that a lightning protection system may be required for multiple prop-rotor blade tips. On the other hand, the lift-cruise type Pegasus, in which the wing tip functions as a vertical tail wing, may require a lightning protection system for the wing tip and the outermost prop-rotor blade tip. Lastly, in the Nexus 4EX model to which a duct is applied, the initial lightning attachment area was not formed on the prop-rotor blade in either the BVP or IVP approaches. Instead, a lightning protection system may be required on the top of the duct and on the vertical tail.

The rotor blade is specified in the lightning certification regulations AC 27-1B [120] and AC 29-2C [121] as a major component that must be protected from fatal damage by the direct effects of lightning on the rotorcraft. This is not limited to rotorcraft, for example, but also applies to UAM aircraft, which are undergoing miniaturization in various forms. Actually, lightning can have more fatal consequences for the prop-rotor blades of a UAM aircraft.

Zones 1A and 1B, identified in the electrostatic potential simulation results of four representative UAM aircraft, are summarized in Table 4. These results indicate the electrostatic potential simulation model can be used to identify the initial lightning attachment area of a new aircraft configuration. In addition, it can be used to determine the necessary applications of the lightning protection system.

Table 2 Three-dimensional model of four representative UAM aircraft.

Type		**Configuration**
Wingless	Multi-copter (Volocopter 2X)	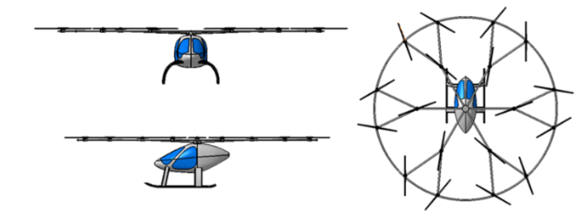
Winged	Lift+cruise (Boeing Pegasus)	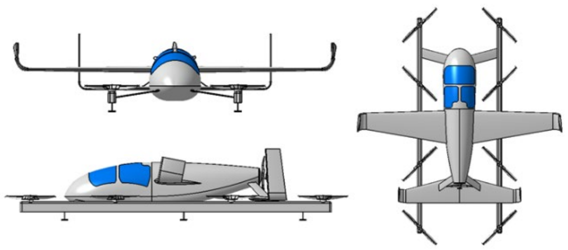
	Vectored thrust (Hyundai S-A1)	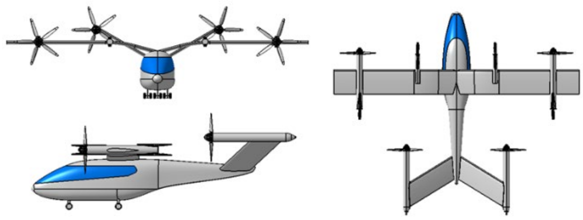
	Vectored thrust (Bell Nexus 4EX)	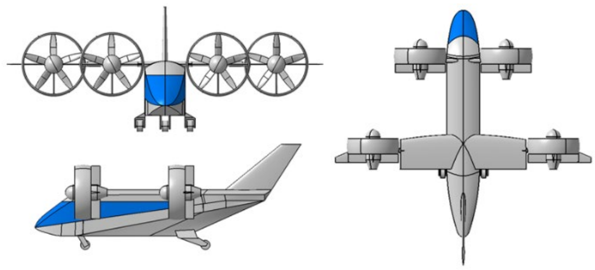

Table 3 Main specifications of the three-dimensional model.

	Length (m)	**Width (m)**	**Height (m)**
Volocopter 2X	3.2	9.15	2.15
Pegasus	9.14	8.53	1.95
S-A1	15	10.7	4.3
Nexus 4EX	12.2	12.2	4.8

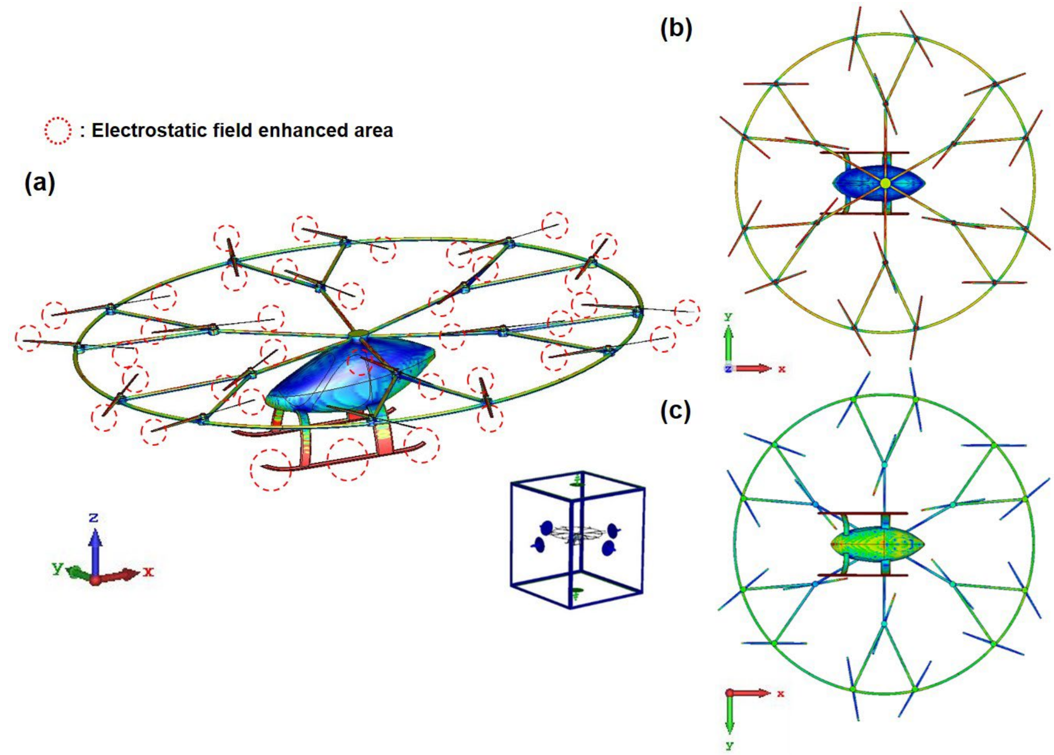

Fig. 12. Electrostatic field distribution of Volocopter 2X (BVP): (a) perspective; (b) top view; (c) bottom view.

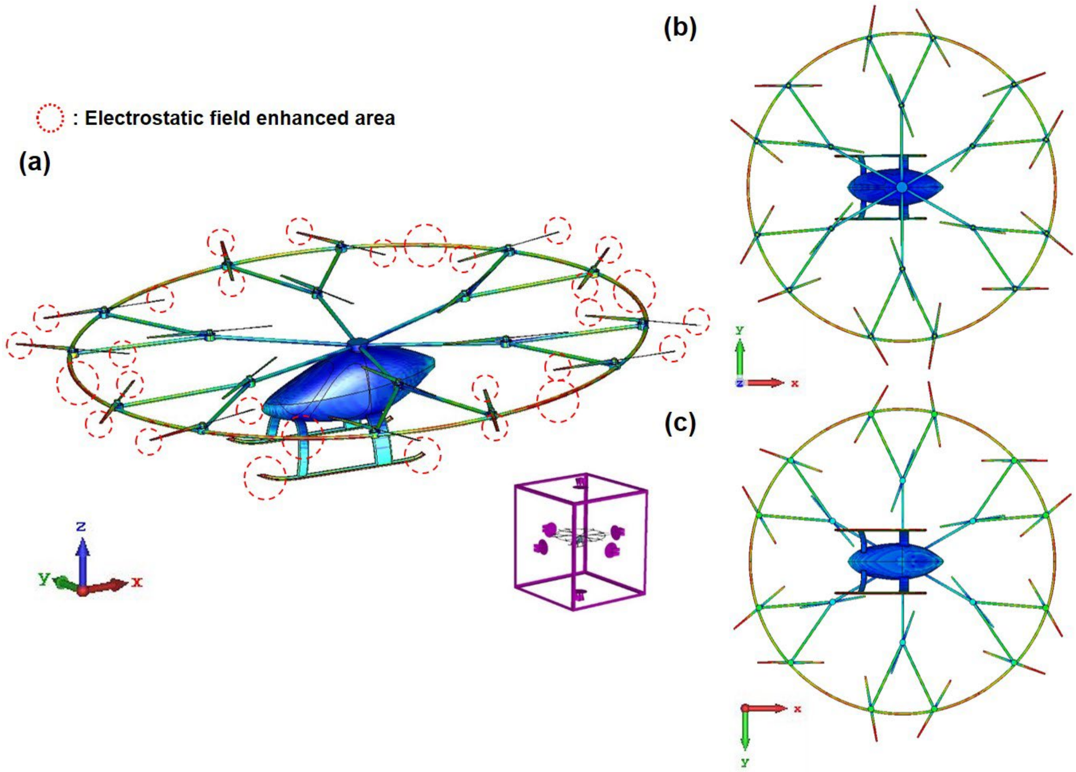

Fig. 13. Electrostatic field distribution of Volocopter 2X (IVP): (a) perspective; (b) top view; (c) bottom view.

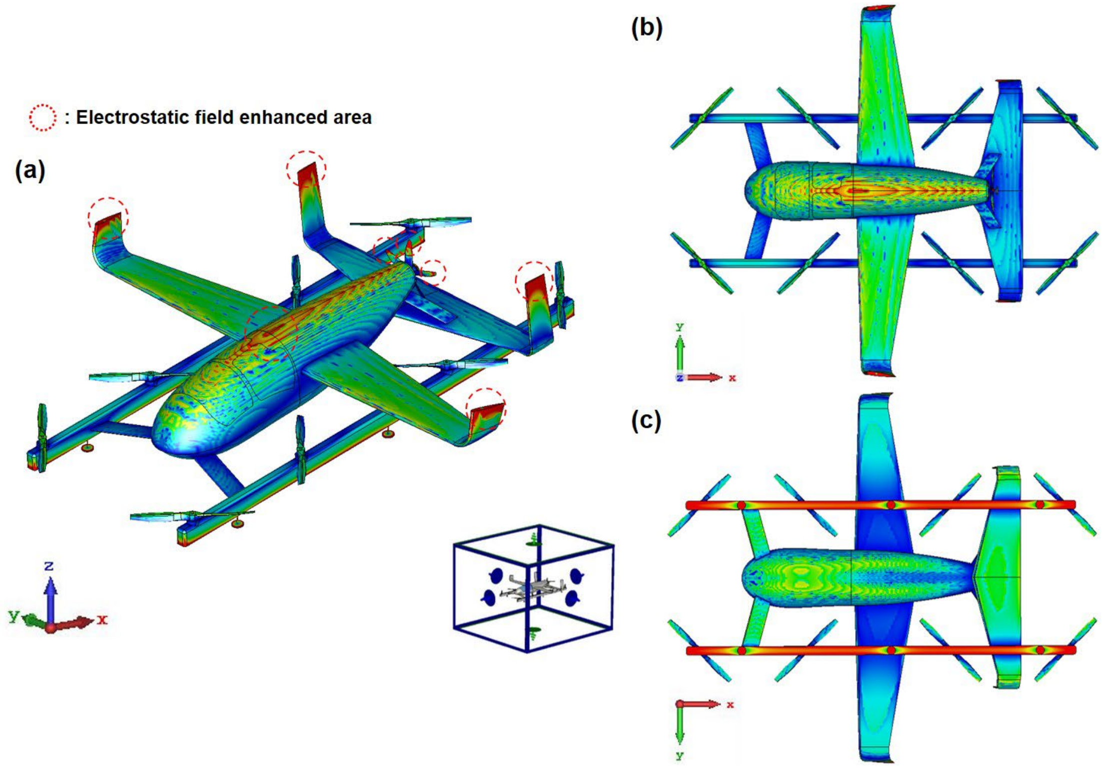

Fig. 14. Electrostatic field distribution of Pegasus (BVP): (a) perspective; (b) top view; (c) bottom view.

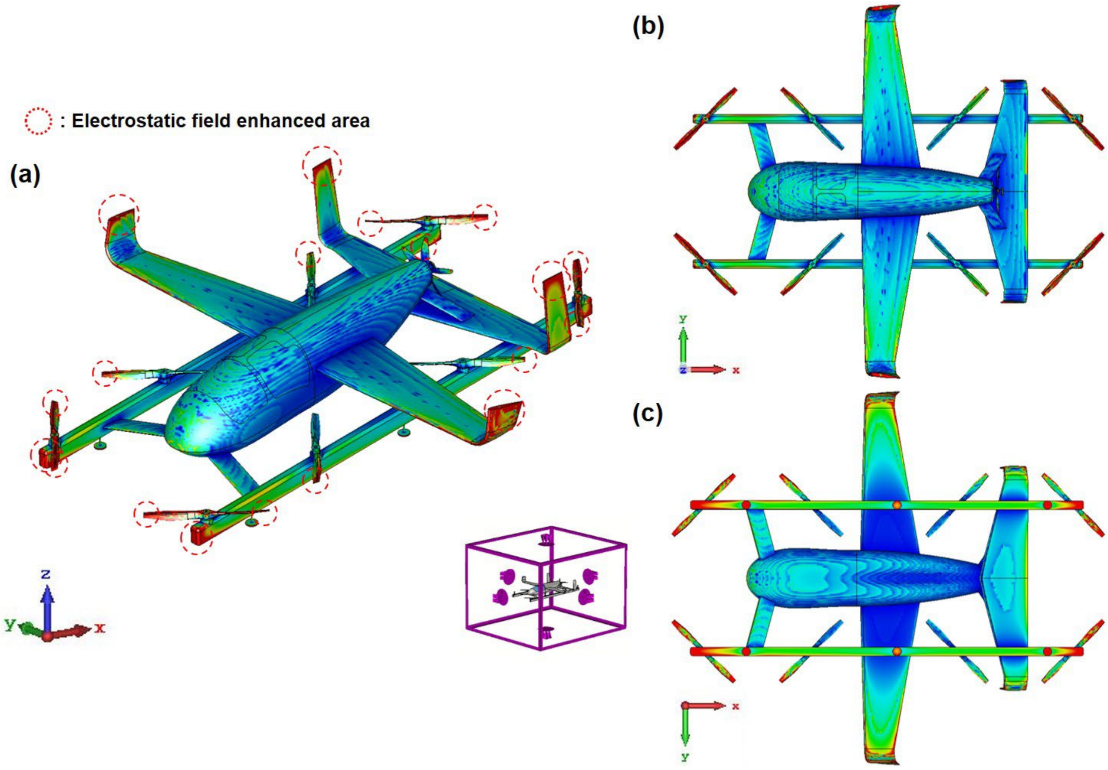

Fig. 15. Electrostatic field distribution of Pegasus (IVP): (a) perspective; (b) top view; (c) bottom view.

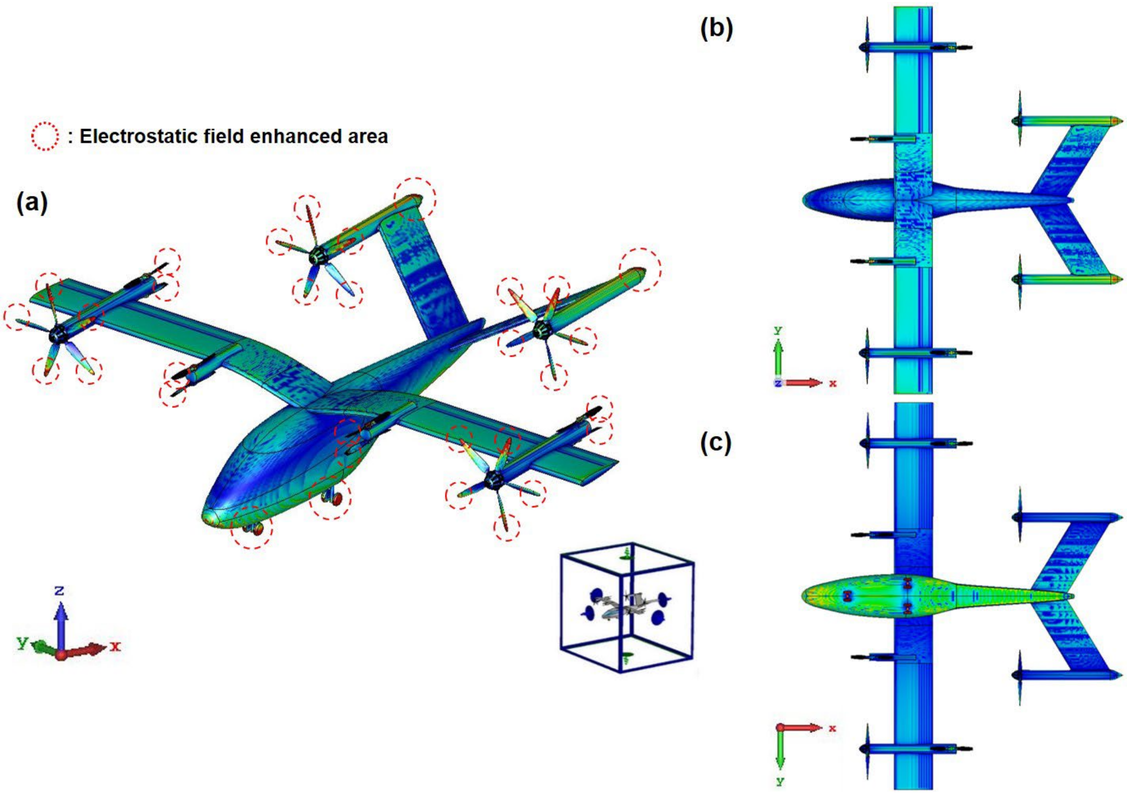

Fig. 16. Electrostatic field distribution of S-A1 (BVP): (a) perspective; (b) top view; (c) bottom view.

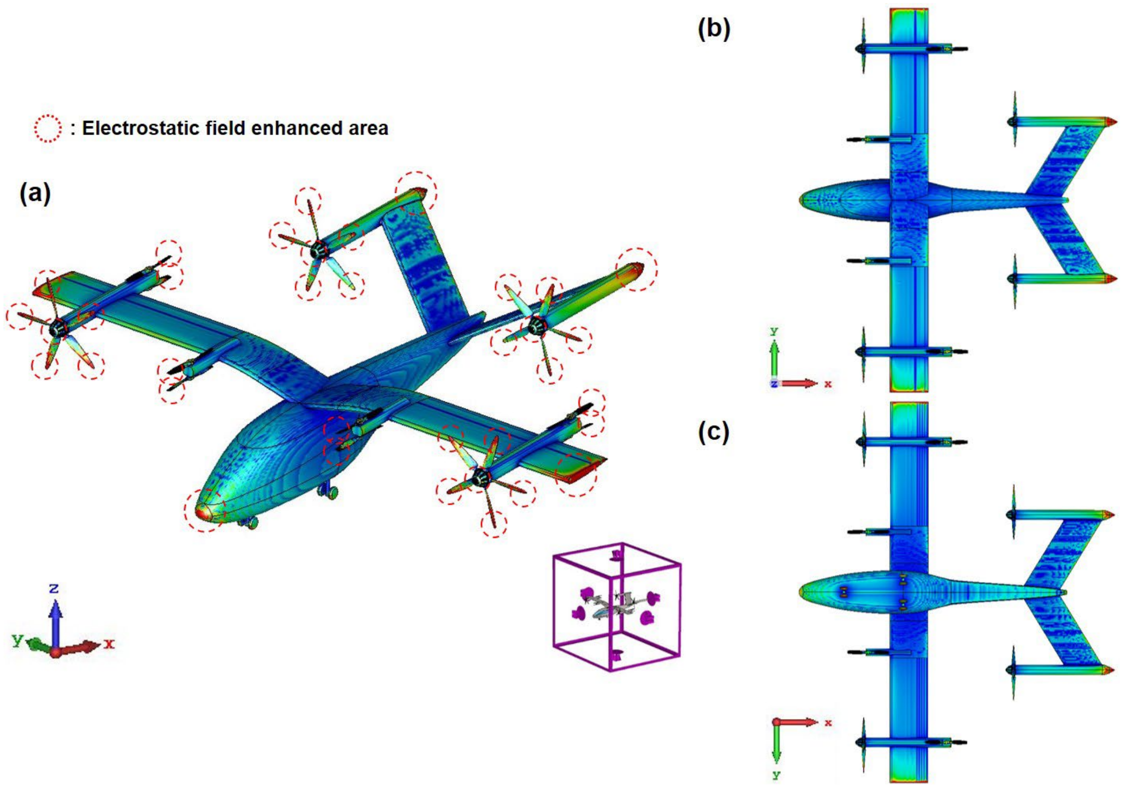

Fig. 17. Electrostatic field distribution of S-A1 (IVP): (a) perspective; (b) top view; (c) bottom view.

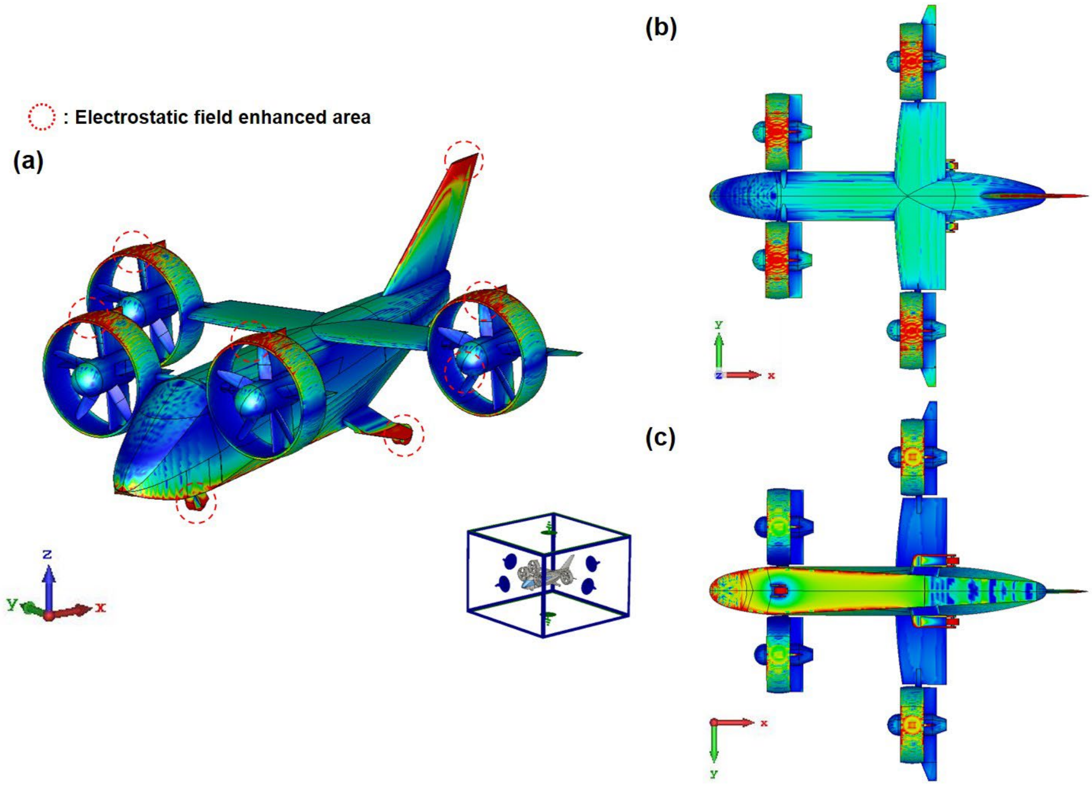

Fig. 18. Electrostatic field distribution of Nexus 4EX (BVP): (a) perspective; (b) top view; (c) bottom view.

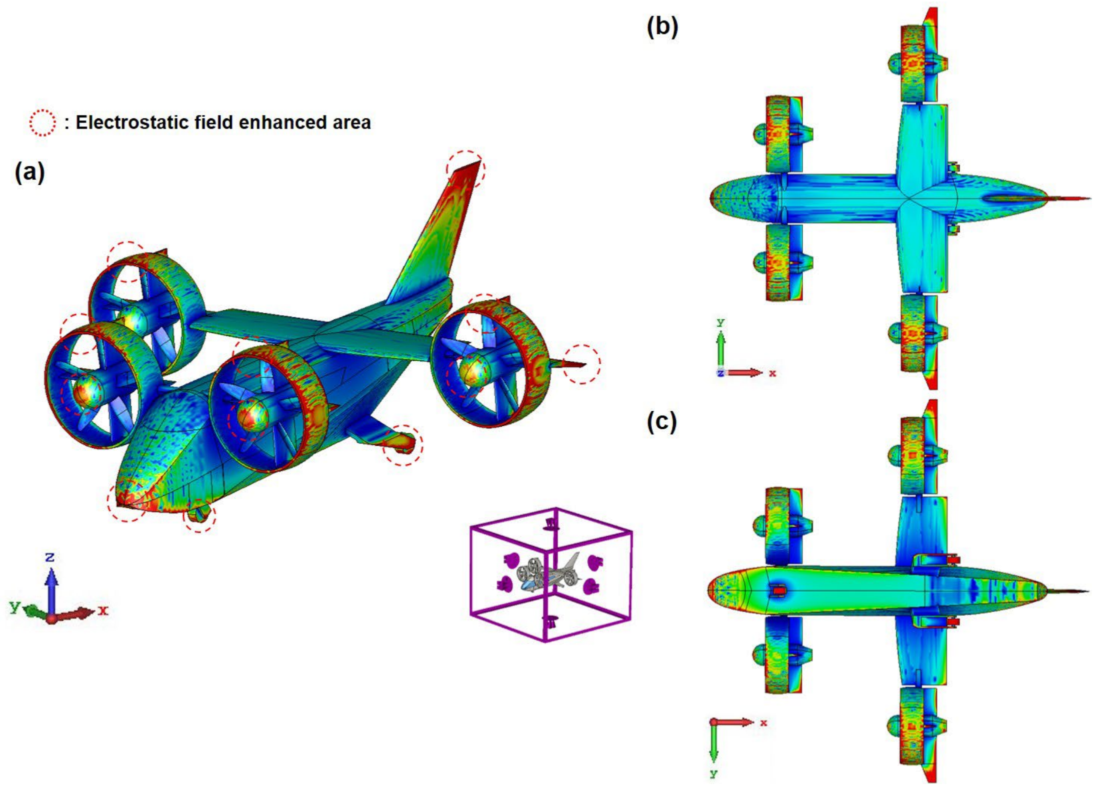

Fig. 19. Electrostatic field distribution of Nexus 4EX (IVP): (a) perspective; (b) top view; (c) bottom view.

Table 4 Summary of lightning initial attachment zones by configuration.

Type		Approach	Zone 1A, 1B
Wingless	Multi-copter (Volocopter 2X)	BVP[a]	Prop-rotor blade tip, support frame, landing skid
		IVP[b]	Prop-rotor blade tip and support frame on the outside around the rotor hub, landing skid tip and bottom
Winged	Lift+cruise (Boeing Pegasus)	BVP	Push prop-rotor blade tip, main wing winglet, horizontal tail wing winglet, upper fuselage, support frame, landing gear bottom
		IVP	Prop-rotor blade tip, push prop-rotor blade tip, main wing winglet, horizontal tail wing winglet, support frame tip, landing gear bottom
	Vectored thrust (Hyundai S-A1)	BVP	Tilt prop-rotor blade tip, stacked prop-rotor blade tip, overall landing gear, tail blade tip
		IVP	Tilt prop-rotor blade tip, stacked prop-rotor blade tip, prop-rotor cone, main wing tip, tail wing tip, nose, landing gear bottom
	Vectored thrust (Bell Nexus 4EX)	BVP	Duct top, vertical tail wing tip, landing gear
		IVP	Nose, overall duct, prop-rotor cone, main wing tip, vertical tail wing tip, landing gear

[a] Electric potential specified on outer boundary.
[b] Electric potential specified on aircraft.

3. Direct effects of lightning on a UAM prop-rotor blade: experimental study

3.1. Specimen preparation

The lightning zoning analysis in Section 2 showed that prop-rotor blade tips could be identified as Zone 1A, an area which has a high probability of initial lightning attachment. An experimental study was conducted on the direct effects of lightning on a prop-rotor blade specimen. A woven carbon/epoxy blade consisting of Dowaksa A-38 carbon fibers with 3K and 6K tow with 2 x 2 twill weave [81, 92, 122-126] was used. Dk-118 was used as the resin and hardener for the epoxy resin. Compared to carbon/epoxy, a woven carbon/epoxy can more easily produce complex shapes such as prop-rotor blades. Woven carbon/epoxy laminate is made by wet lay-up processing. Woven carbon/epoxy laminate consists of eight layers in the fill direction. It was laminated in order from the skin, to 3 plies of 3K fiber and 5 plies of 6K fiber. The specimen was cured for 4.5 hours at a temperature of 120 degrees and a pressure of 4.4 bar in the autoclave. The fiber volume fraction was 60 percent.

To conduct the lightning experiments, two samples of the woven carbon/epoxy laminate measuring 210mm x 180mm were produced. The 3K and 6K fibers were 0.3mm and 0.4mm, respectively, per each ply. The total thickness of the specimen was about 2.9mm.

3.2. Jig preparation and experimental setup

The lightning test was conducted using the high impulse current generator (ICG) of Korea Electric Power Research Institute to assess the direct effect of a lightning strike on the prop-rotor blade. The impulse current device, an instrument that generates high current, is usually used in specimen-unit experiments. The lightning test jig and setup for generating the lightning strike are shown in Fig. 20 [127, 128]. The top and bottom plates of the test model (500mm x 500mm) were made of glass fiber/epoxy for insulation. Four rods (with 40mm length) supporting the top and bottom plates were also made of glass fiber/epoxy. The probe (with a diameter of 8mm) and the specimen-positioning plate (350mm x 350mm) were made of stainless steel and titanium, respectively. The metal probe and plate were connected to the impulse current generator by ground.

The main current generated from the impulse generator directly charges the probe. When the probe is charged with more than a certain amount of current, an insulation fracture occurs, causing the main current to flow from the probe to the specimen. Lightning was applied to the central region of the specimen from the discharge electrode probe. The gap between the surface of the specimen and the end of the probe was fixed at 2mm for all tests [127, 128].

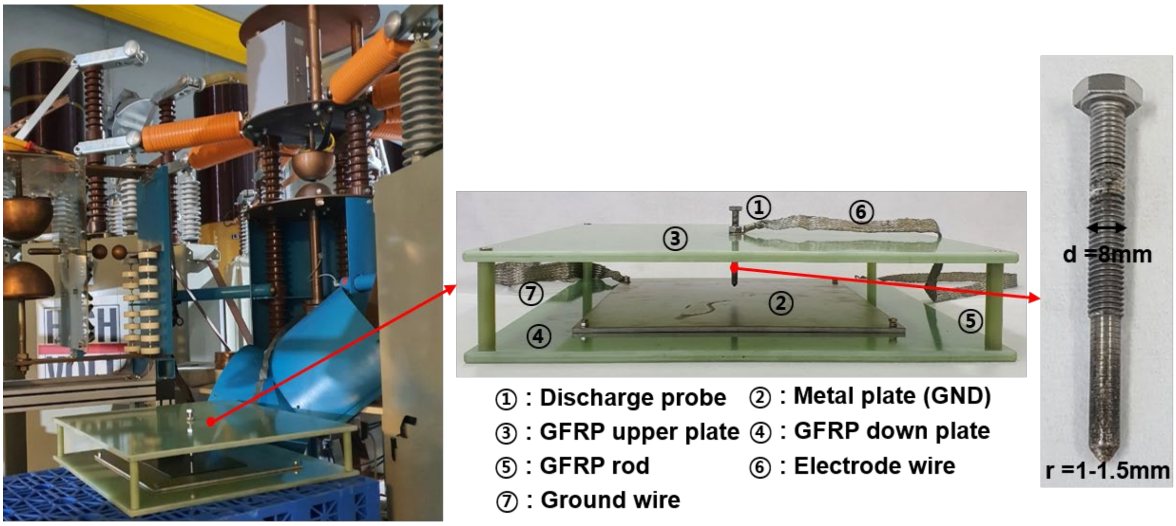

Fig. 20. Lightning test setup.

3.3. Lightning current waveform

The aerospace recommendation practice, SAE ARP 5412B, provides a lightning current waveform for lightning testing, as shown in Fig. 21 [99]. Aircraft lightning waveforms consist of A, B, C, D, and H waveforms, depending on the lightning environment. All waveforms are defined in the time domain and are defined as double exponential functions, except C, as follows,

$$I(t) = I_0(e^{-\alpha t} - e^{-\beta t}), \tag{5}$$

where I_0 is the current constant associated with the peak current magnitude. The values α and β represent the reciprocal of the wave tail time constant and the reciprocal of the wave front time constant, respectively. The exponential current waveform equation can also be explained by front time (T1) and tail time (T2) where T1 represents the time from 10 percent to 90 percent of the maximum current, and T2 represents the time to half of the maximum current.

The component A waveform used in the test simulates the first return stroke, which may vary with the flight altitude of the aircraft. The component A waveform has the highest peak current value among all the waveform currents, and its duration is less than 500μs. Because it delivers enormous energy in a short period of time, it can inflict explosive damage.

The area of fiber damage and depth of damage are mainly determined by the lightning peak current.

The thermal decomposition and delamination of the resin associated with internal damage are determined by the amount of electrical charge (Q) and the energy defined by the action integral (AI) of the lightning [87], which are defined as

$$Q = \int_0^t i(t)\,dt\,, \tag{6}$$

$$AI = \int_0^t i(t)^2\,dt\,. \tag{7}$$

The level of lightning can be classified by peak current, as summarized in Table 5. To compare the fracture at the two lightning levels requiring repair, a 7.6/17.7μs waveform with peak current 39.7kA and an 8.1/18.6μs waveform with peak current 80.7kA were used in the test.

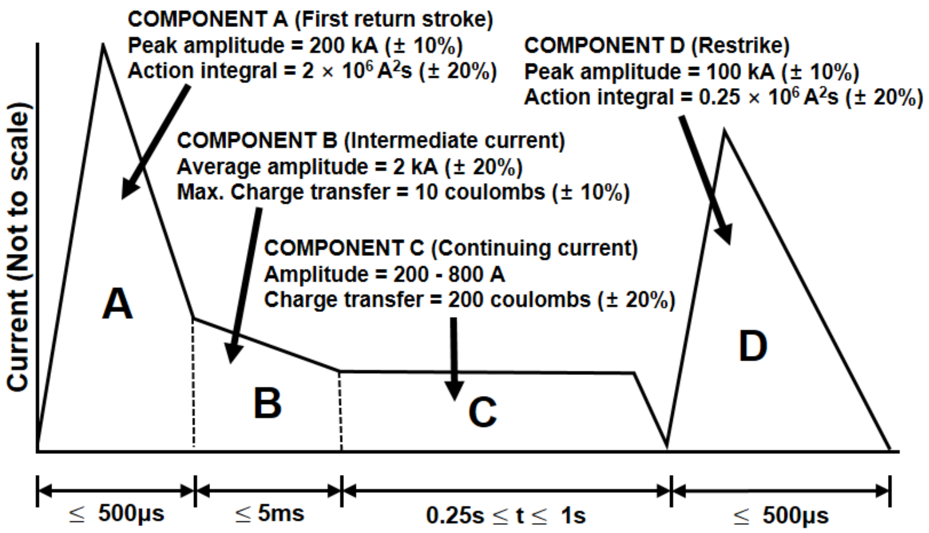

Fig. 21. Lightning standard current waveform [99].

Table 5 Typical lightning strike levels [100].

Threat	Criteria	Requirement
High energy strike	Rare lightning strike 50-200 kA	-Striking level in accordance to zoning diagram -Continued safe flight (70 % DLL)
Intermediate energy strike	Medium lightning strike 30-50 kA	-Repair needed (100 % DLL) -Visible damage
Low energy strike	Nominal lightning strike 10-30 kA	-No repair needed (150 % DLL) -Non or barely visible damage

4. Direct effects of lightning on a UAM prop-rotor blade: numerical simulation

4.1. Thermal damage due to joule heating

Joule heating refers to the process that occurs when a current passing through a conductor generates heat by resistance. It is also called Ohmic heating or resistive heating [129, 130]. In this process, the following charge conservation equation holds

$$\frac{\partial \rho_e}{\partial t} + \nabla \cdot \mathbf{J} = 0, \tag{8}$$

where ρ_e is the charge density and $\mathbf{J}$ is the internal current density. The relationship between current and Joule heat can be expressed as follows (σ^E being electrical conductivity),

$$P_{ec} = \mathbf{J} \cdot \mathbf{E} = \frac{J^2}{\sigma^E}. \tag{9}$$

P_{ec} represents the amount of heat energy generated by the resistance of the current flowing through the conductor.

On the other hand, heat transfer in a media follows Fourier's law. The governing equation of heat balance can be expressed as follows,

$$\rho C_p \frac{\partial T}{\partial t} = \nabla \cdot (k \nabla T) + \frac{\mathbf{J}^2}{\sigma^E}, \tag{10}$$

where C_p is the specific heat capacity at constant pressure, ρ is the density, T is the absolute temperature, and k is the thermal conductivity.

4.2. Lightning arc channel expansion

After assuming that lightning current flows along a cylindrical plasma channel, Braginskii [101] proposed the change in the lightning current with time in the arc channel radius, as follows,

$$R(t) = \alpha \rho_0^{-1/6} I(t)^{1/3} t^{1/2}, \tag{11}$$

where $R(t)$ is the radius (m) of the arc channel at time t (sec), α is a constant with α = 0.294, ρ_0 is the air density at atmospheric pressure, ρ_0 = 1.29kg / m^3, and $I(t)$ is the current value (A) in time t. However, it turns out that Eq. (11) is not suitable for estimating the channel radius during the attenuation of the Component A waveform. After many experimental and numerical studies, an arc channel radius model closer to the actual lightning waveform was proposed [103-105]. A value of α = 0.097 and simplification of $I(t)$ by I_{peak} were proposed to properly describe the continuous arc expansion occurring even while the current decreases following the lightning peak current [102],

$$R(t) = 0.097 I_{peak}^{1/3} t^{1/2}. \tag{12}$$

After several experimental and theoretical studies [106, 107], the current density $J(r,t)$ of the lightning arc channel was shown to have a Gaussian distribution with a maximum value at the center of the channel as follows,

$$J(r,t) = J_{\max}(t) e^{-cr^2}, \; r \leq R(t), \tag{13}$$

where r is the radius coordinate (m), and c is a constant based on the relation that the current density at $r = 0.55R$ is equal to 10 percent of $J_{\max}(t)$ from the heat flux distribution [107],

$$c = -\frac{\ln(0.1)}{(0.55 \cdot R(t))^2}. \tag{14}$$

The function $J_{\max}(t)$ was determined using the relation that the current density integration over the circular region is equal to the total current of the lightning channel $I(t)$ [108, 109], as follows,

$$J_{\max}(t)=\frac{I(t)}{\int_0^{2\pi}\int_0^{R(t)} re^{-cr^2}\,drd\theta}. \tag{15}$$

The heat flux of the lightning arc transmitted to the surface of the anode structure is expressed as [131],

$$Q=J(U_a+\Phi_{mat}+\frac{5k_b}{2\varepsilon}(T_{arc}-T_{anode})). \tag{16}$$

Here J is the current density (A/m^2), U_a is the anode voltage drop (4–5V), Φ_{mat} is the work function of the material (4–5V), T_{arc} is the arc temperature, T_{anode} is the anode temperature, and k_b is the Boltzmann constant, and ε is the electron electrical charge. The third term on the right-hand side represents a negligible change in the electro-kinetic energy of the anode structure for high current [131]. If this term is neglected, the heat flux of the lightning arc $Q(r,t)$ is reduced to

$$Q(r,t)=10J(r,t). \tag{17}$$

4.3. Geometry and materials properties

When a composite material is struck by lightning, it may be thermally damaged by resistance heat. As the temperature increases, the matrix changes first, and when exposed to higher temperatures, the composite fibers begin to change [87-91, 129, 130]. The epoxy resin constituting the carbon/epoxy laminate is very sensitive to thermal energy. Damage to the epoxy resin may lead to structural deterioration and damage, which may eventually lead to an accident. To describe the temperature effect on the composite material, it is necessary to perform a coupled electric-thermo computational simulation.

Several studies have been performed to predict the impact and damage to the carbon/epoxy laminate due to lightning strikes [87-91, 129, 130]. Carbon/epoxy materials used in previous simulations have almost similar room temperature and high temperature properties and fiber volume fraction (60–65percent) [132]. The predicted thermal damage regions of these carbon/epoxy composites were found to be similar to each other and to be consistent with the experimental observations [87-91, 124-126, 129, 130].

In this study, a woven carbon/epoxy having room temperature characteristics similar to the one used in the study of Duong *et al*. [130] were used. Woven carbon/epoxy laminate has the same thermal and electrical conductivity in the longitudinal and transverse directions [133]. Table 6 shows the properties of woven carbon/epoxy laminate up to 3589K (fiber sublimation temperature). When the local temperature exceeded 3589K, the rest of the simulation was updated locally with the properties of the composite material valid above 3589K [130]. The combined latent heat of fusion and vaporization in the finite element model were assumed to be 4.8×10^3 kJ/kg and 4.3×10^4 kJ/kg, respectively [90]

Table 6 Material properties of the woven carbon/epoxy laminate [130].

Temp. T (K)	**Density ρ (kg/m³)**	**Specific heat Cp (J/kg·K)**	**Thermal conductivity**		**Electrical conductivity**	
			Long. k_{11}, k_{22} (W/m·K)	**Thick. k_{33} (W/m·K)**	**Long. σ_{11}, σ_{22} (S/m)**	**Thick. σ_{33} (S/m)**
298	1480	1065	8	0.67	34120	0.00341
616	1480	2100	2.608	0.18	34120	0.00341
773	1020	2100	1.736	0.1	34120	0.0020
783	1020	1700	1.736	0.1	34120	0.0020
1273	1020	1900	1.736	0.1	34120	0.0020
3589	1020	2509	1.736	0.1	34120	0.0020
>3589	1020	5875	1.015	1.015	200	1.0E+09

4.4. FEM modeling and boundary conditions

In this study, COMSOL's electric-thermal model [134] was used to predict the damage area caused by lightning striking a woven carbon/epoxy laminate with dimensions of 210 mm x 180mm and 8 layers in the fill direction. Based on previous studies related to mesh sensitivity [110], the mesh size should be smaller than 2.5mm near the lightning attachment area. The mesh of the finite element model was densely constructed near the attachment area. As a result, there was a negligible difference between the expected temperature and potential difference. All eight layers were individually modeled to increase the effectiveness of the analysis. The simulated laminates were discretized using 196,017 elements, 164,934 prisms, 23,562 triangles, 6,300 quads, 1,180 edge elements, and 41 vertex elements [135]. A boundary condition was assumed based on the actual lightning test. Figure 22 shows the finite element model and boundary conditions of the thermal radiation and electrical potential.

To simulate the characteristics of lightning applied to the specimen, the change in arc channel expansion over time was applied in the center of the top of the model [101-111]. The initial condition of the specimen was set to 298K, which is an ambient temperature condition. Since the titanium plate under the specimen floor was electrically grounded, the specimen floor was assumed to be zero. The potential of the side was assumed to be zero because an electric discharge from the side to the bottom titanium plate was observed during all lightning experiments.

Thermal radiation was applied to the top and sides of the specimen, and the bottom surface was assumed to be adiabatic. The rise in temperature at the bottom was neglected because it was close to zero. The surface emissivity of the laminate was assumed to be 0.9 [90]. Since a lightning strike occurs for an extremely short period of time, convective heat transfer around the specimen was not considered. In addition, the contact properties were not considered because a perfect bond between thin laminas was assumed [110, 129].

The purpose of this study is to identify the tendency of thermal damage caused by a lightning strike to composite materials (carbon/epoxy) used in prop-rotor blades of UAM aircraft. The present study was conducted similarly to the direct lightning tests reported in the previous studies [87, 127, 130]. To simulate the characteristics similar to artificial lightning applied to the specimen, the change of arc channel expansion with time was applied to the center of the uppermost part of the model. The present setup in the simulation differs in some ways from the test setup described in SAE ARP 5416. For example, the arc/current flow was not induced to a specific point, and the component A reduced waveform with the strongest intensity was used as the initial lightning waveform.

Figure 23 shows the local linear approximation of the impulse current information of the waveform fed to COMSOL as a function of time. The surface current was uniformly applied only inside the spatially and temporally varying circular lightning arc channels for 25μs and 28.5μs.

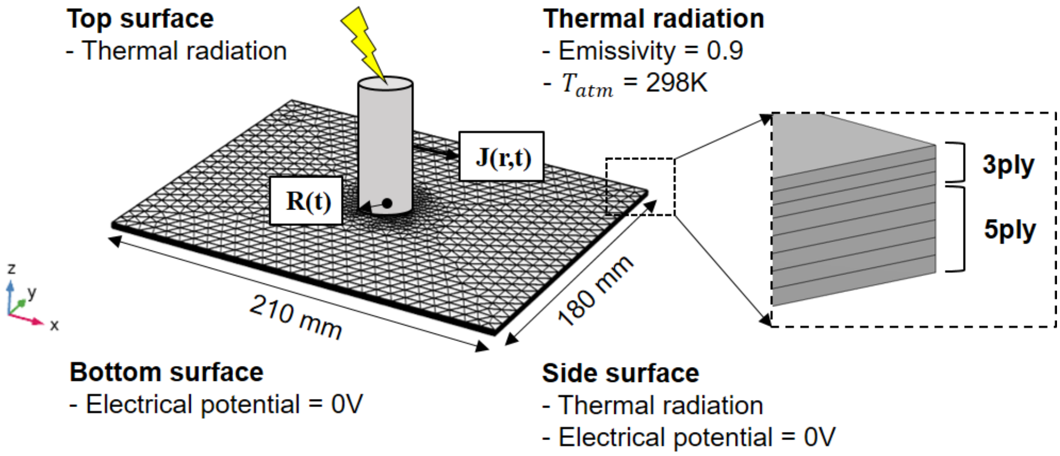

Fig. 22. Finite element model and boundary conditions.

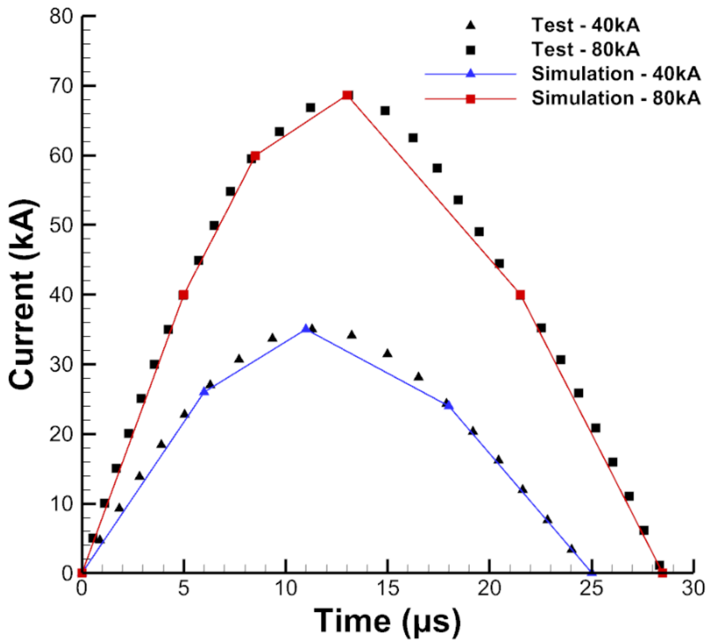

Fig. 23. Lightning current waveform in test and simulation.

5. Results and discussion

5.1. Experimental results

A lightning test was conducted on a 210mm x 180mm woven carbon/epoxy laminate to compare the degree of damage to the prop-rotor blades according to the lightning level. The peak currents of the current waveform actually applied to the specimen, reflecting external factors such as the test environment, were 35.0kA, 8.9/20.2μs, and 68.6kA 9.9/22.6μs. Figure 24 shows the results of surface damage to the top of the specimen, visually identified after the high current impulse test. Overall, the difference in the degree of damage caused by current intensities of 35.0kA and 68.6kA can be compared.

In the woven fiber material with the same electrical and thermal properties in the warp and fill directions, currents penetrated in both directions and generated high resistance heating and resin pyrolysis, and ultimately formed a near-circular damage area as a hole. Typical damage profiles related to fiber and matrix damage were quantified using image processing. Nondestructive testing was performed using a micro X-ray inspection system (InspeXio SMX-225CT, Shimadzu, Japan) to determine internal damage in terms of the damage area and depth. The damage area and depth were determined by imaging the top and cross sections of each specimen using an X-ray CT, as shown in Figs. 25-26. After performing image processing using the viewer program of the X-ray CT scan system, the darkened area compared to the top section was determined as the damaged area. Then, the depth was measured using the length measurement tool of the viewer program.

Table 7 summarizes the damage area and depth caused by lightning strikes on each of the two laminates. Since the damage area of the top section was not perfectly circular, the diameter of the damage area changed slightly depending on the direction. In case 1, 1.3% of the area was damaged compared to the uppermost area, and in case 2, 2.7% was damaged. In addition, in case 1, 34.5% of the depth was damaged, and in case of case 2, 45.5% was damaged. Compared to case 1, the damage area and depth in case 2 increased by 103.6% and 32.0%, respectively.

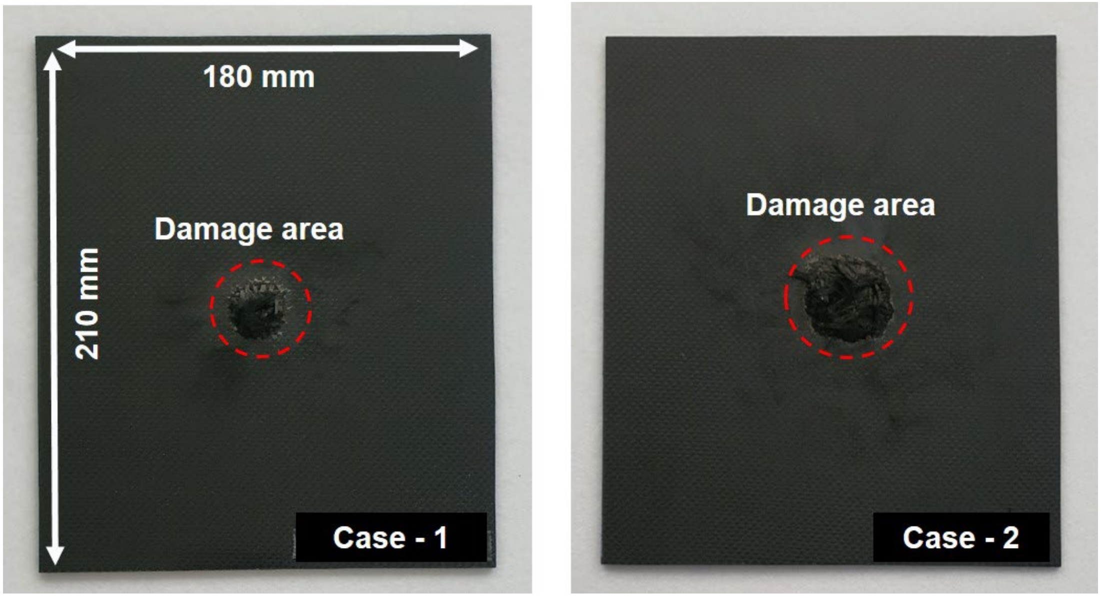

Fig. 24. Lightning test results: case 1 (40kA); case 2 (80kA).

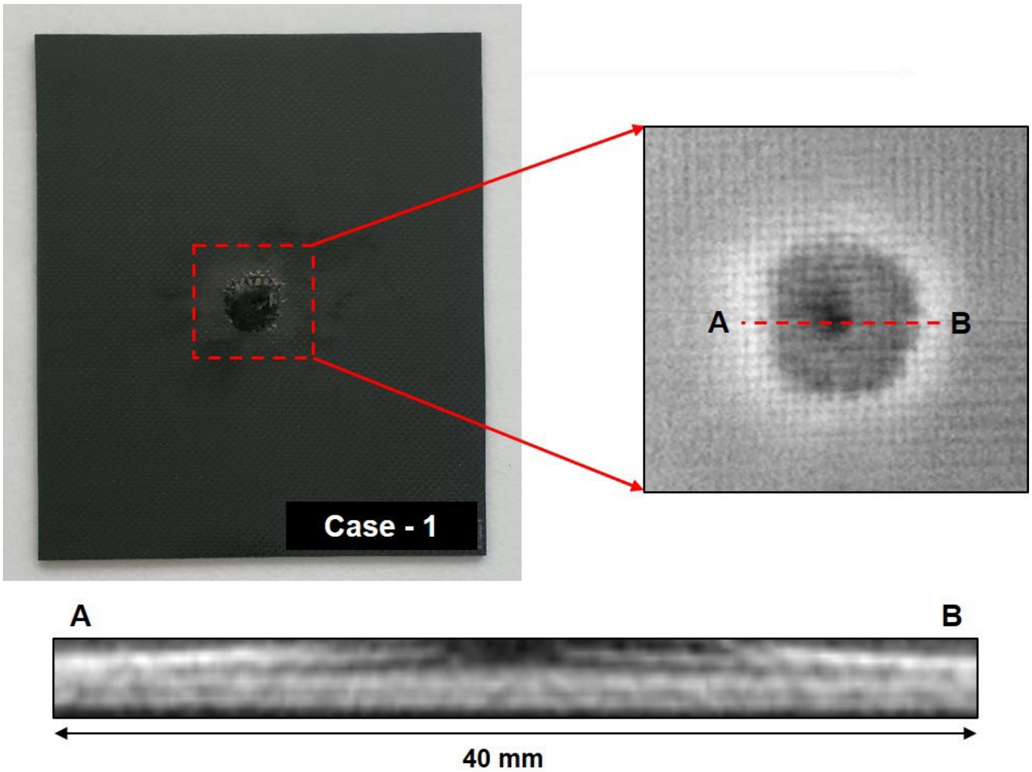

Fig. 25. X-ray CT scan result of case 1.

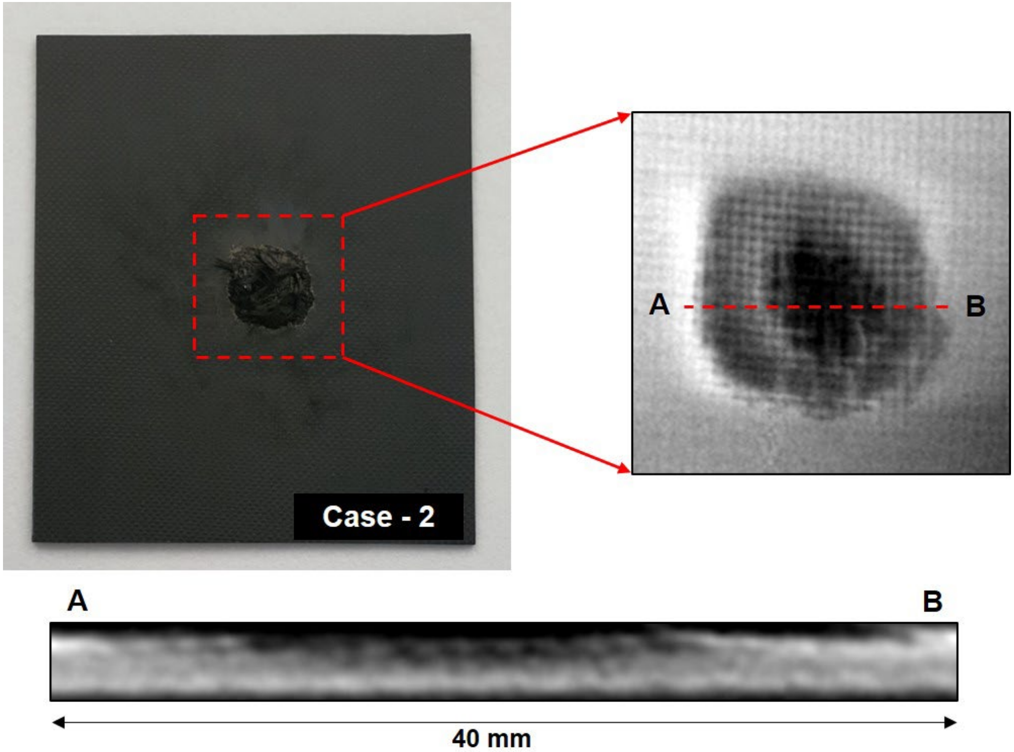

Fig. 26. X-ray CT scan result of case 2.

Table 7 Experimental conditions and damage region after lightning strikes on the specimen.

	Setting peak current (kA)	Real peak current (kA)	Charge transfer (C)	Action integral (A^2s)	Damage area (mm^2)	Damage depth (mm)
Case 1	40	35.0	0.5478	15100	452	1.00
Case 2	80	68.6	1.1659	64188	1024	1.32

5.2. Simulation results

A coupled electrical-thermal simulation using COMSOL was performed on a 210 x 180 mm woven carbon/epoxy laminate model to compare the degree of damage to the prop-rotor blades according to the lightning level. The occurrence of local Joule heating and irreversible matrix decomposition damage related to various material properties was predicted. The region where the temperature reached 573–773K in the coupled electrical-thermal simulation was defined as the epoxy matrix decomposition region [110, 130]. Typical epoxy matrices undergo thermal decomposition in the temperature range of 573–773K, while carbon fiber sublimation occurs at 3589K [87-90]. Epoxy matrix damage occurs first at high temperatures, followed by carbon fiber damage at much higher temperatures where sufficient oxygen is available for a long enough time. Therefore, in the lightning attachment area, an extensive epoxy matrix damage area surrounds a highly localized area of intense fiber damage.

Figure 27 shows the predicted temperature distribution in the top and cross section due to lightning strikes on each of the two laminates. Figures 28 and 29 show the changes in the damage area and depth over time. Table 8 summarizes the damage area and depth. In case 1, 1.4% of the area was damaged compared to the uppermost area, and in case 2, 2.5% was damaged. In case 1, 33.8% of the depth was damaged compared to the thickness, and in case 2, 43.8% was damaged. Compared to case 1, the damage area and depth of case 2 increased by 75.1% and 29.6%, respectively.

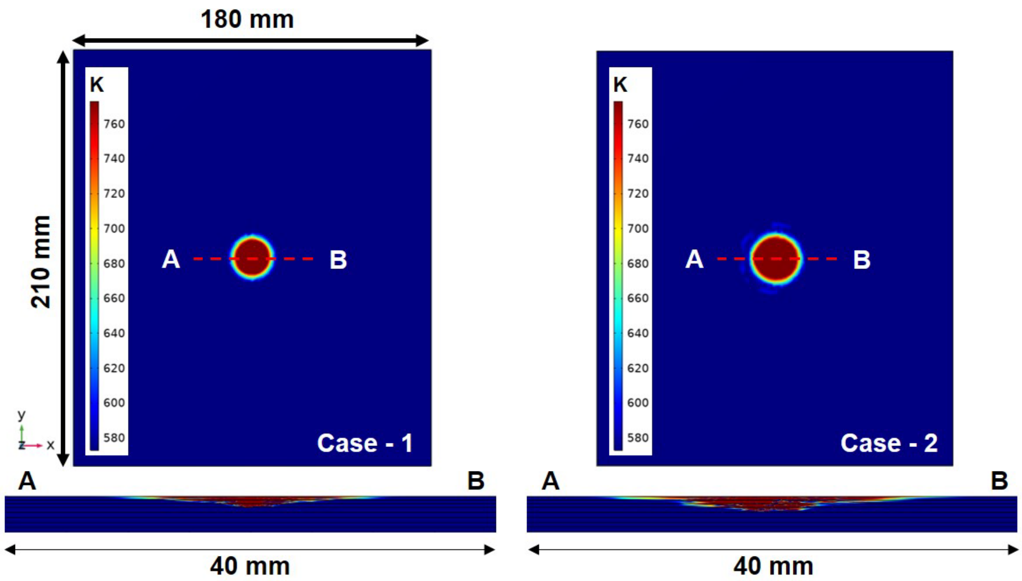

Fig. 27. Temperature distributions of laminates: left (40kA); right (80kA).

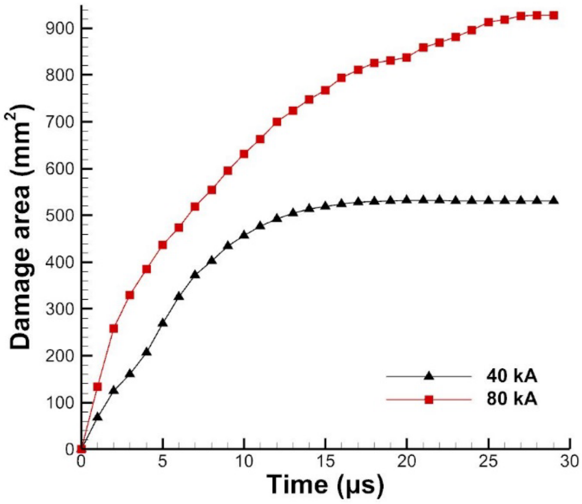

Fig. 28. Prediction of the damage area.

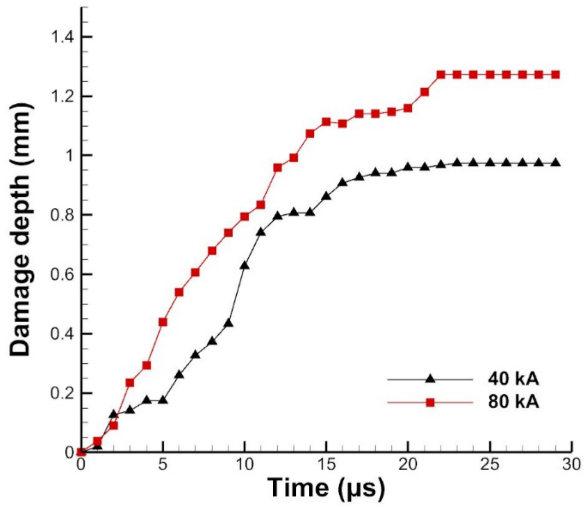

Fig. 29. Prediction of the damage depth.

Table 8 Damage area and depth from the numerical simulation on the laminate model.

	Damage area (mm^2)	Damage depth (mm)
40 kA	530	0.97
80 kA	928	1.27

As mentioned in the introduction, when comparing the rotor blades of rotorcraft and the prop-rotor blades of UAM aircraft, size is the most important factor affecting lightning strike characteristics. Therefore, two blades with different chord lengths were modeled and the degree of damage due to lightning strike was compared. The coupled electric-thermal numerical simulation predicted the occurrence of local Joule heating and irreversible matrix decomposition damage.

Figure 30 shows the temperature distributions in curved top surface of the prop-rotor and rotor blades with a cross section of NACA 0012, respectively, due to lightning strikes. The damaged areas of the uppermost area were 257mm^2 and 272mm^2, respectively, resulting in 2.57m (257/100) and 0.91m (272/300) in reference to the length of the chord. From this result, it can be expected that the prop-rotor blade of a relatively small UAM aircraft will suffer more damage even after being struck by lightning of the same intensity.

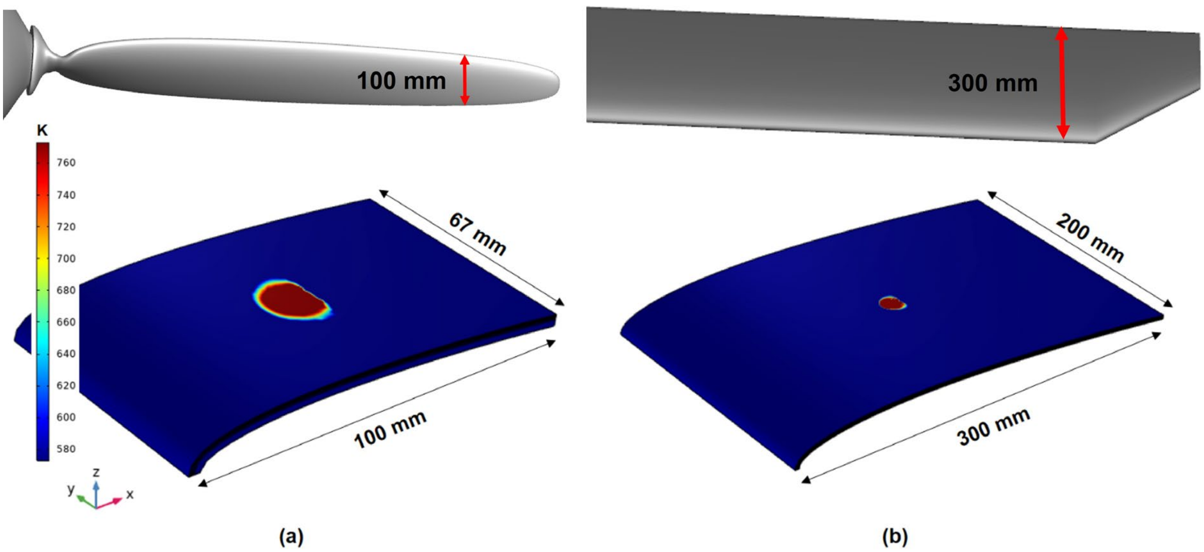

Fig. 30. Comparison of damage area: (a) prop-rotor blade; (b) rotor blade.

5.3. Comparison of experimental and simulation results

To evaluate the accuracy of the lightning simulation model, the damage area and pattern obtained by experiments and simulations were compared. Figures 31-34 show the thermal decomposition area obtained by visual image, X-ray CT and simulation. When the damaged area and pattern of fibers and matrix were compared according to the lightning strike level, the simulation results were found to agree well with the experimental results obtained by visual image and X-ray CT. Tables 9 and 10 summarize the relative errors between the experimental and simulation results. The relative errors in the surface damaged area due to matrix decomposition were 5.09% and 9.38% in case 1 and case 2, respectively. In addition, the relative errors of the damage depth were 3.00% and 3.79%, respectively. It is believed that these errors are caused by magnetic force, internal expansion pressure, and acoustic shock wave effect, which were not considered in the current computational modeling. It can also be attributed in part to the uncertainty of the electrical and thermal properties used in the simulations.

In general, the damage pattern of the simulation results agreed fairly well with the damage pattern of the experimental results, with less than 10% error. This means that the coupled electric-thermal computational model considering the change in arc channel expansion with time can be effectively used to predict high current damage to composites.

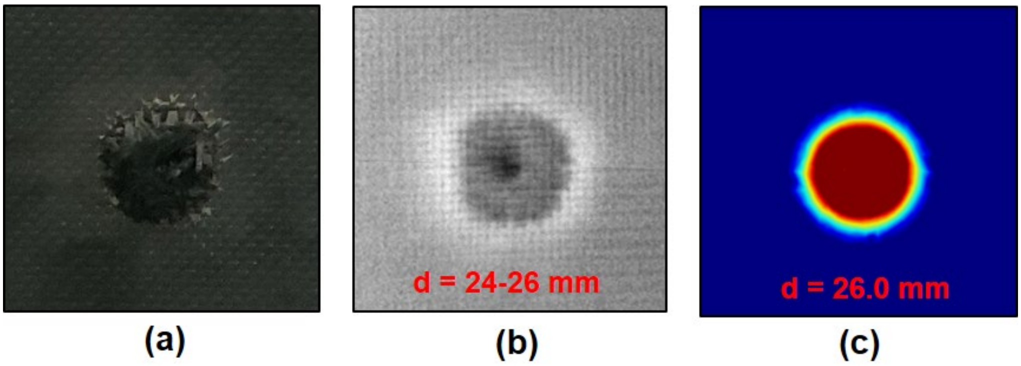

Fig. 31. Comparison of damage area (40kA): (a) visual image; (b) X-ray CT; (c) simulation.

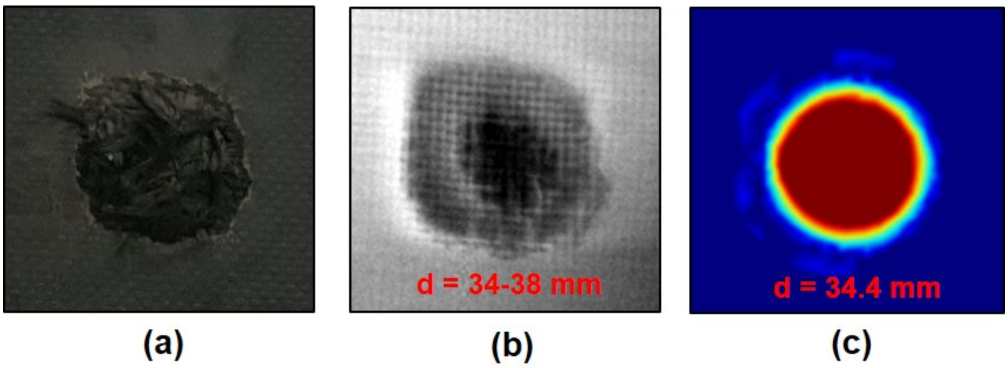

Fig. 32. Comparison of damage area (80kA): (a) visual image; (b) X-ray CT; (c) simulation.

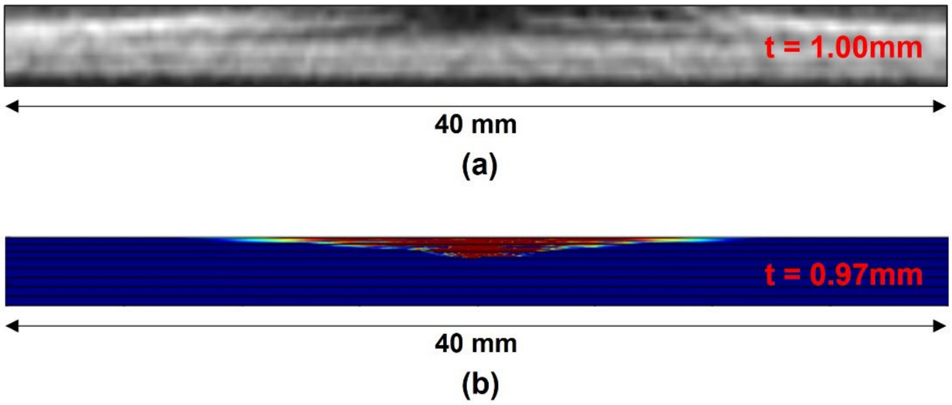

Fig. 33. Comparison of damage depth (40kA): (a) X-ray CT; (b) simulation.

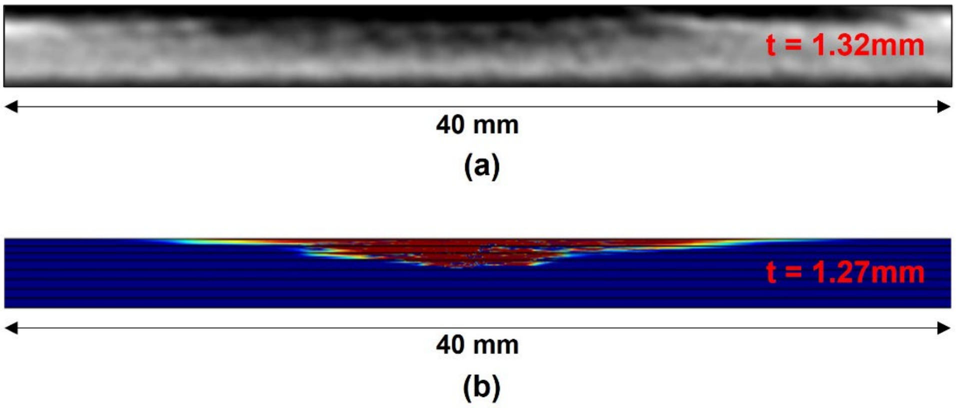

Fig. 34. Comparison of damage depth (80kA): (a) X-ray CT; (b) simulation.

Table 9 Comparison of damage area between experimental and simulation results.

	Experiment visual damage area (mm^2)	**Simulation thermal damage area (mm^2)**	**Relative error (%)**
40 kA	503	530	5.09
80 kA	1024	928	9.38

Table 10 Comparison of damage depth between experimental and simulation results.

	Experiment visual damage depth (mm)	**Simulation thermal damage depth (mm)**	**Relative error (%)**
40 kA	1.00	0.98	3.00
80 kA	1.32	1.27	3.79

6. Conclusion

Among weather-related safety factors such as external air disturbance, hail and icing, lightning strikes are the most dangerous due to the relatively small size of UAM aircraft, and their characteristic flight path, close to the ground. Furthermore, the increasing use of composites for light weight, the adoption of distributed electric propulsion systems to reduce noise, and greater integration and digitization of electronic equipment to make them compact and multi-functional, can cause UAM aircraft to be more vulnerable to lightning strikes. In the event lightning strikes during flights close to the ground or surrounding buildings, it is also difficult to make a safe emergency landing, which can lead to a major accident in the city. Therefore, the commercialization of UAM aircraft without proper lightning protection systems will inevitably be very limited.

In an effort to tackle this problem, this study presents a zoning method for UAM aircraft with complex configurations, and investigated the direct effects of lightning strikes on the prop-rotor blade of UAM aircraft, using both experimental and numerical methods.

First, computational simulation models for zoning analysis were developed for four representative UAM aircraft (one wingless multi-copter, one winged lift/cruise, and two winged vectored thrust types). The initial lightning attachment area formed at the tip of a number of prop-rotor blades in the multi-copter type Volocopter 2X and the vectored thrust type S-A1, implying that a lightning protection system may be required for prop-rotor blade tips.

On the other hand, the lift-cruise type Pegasus was shown to require a lightning protection system for the wing tip and the outermost prop-rotor blade tip. Lastly, the initial lightning attachment area was not formed on the prop-rotor blade, but on the top of the duct and on the vertical tail in the Nexus 4EX model with several ducts enclosing blades.

Next, the lightning zoning analysis identified the prop-rotor blade tips as Zone 1A, which has a high probability of initial lightning attachment. The direct effects of lightning strikes on a prop-rotor blade made of woven carbon/epoxy laminate were investigated using both experimental and numerical methods. In general, the damage pattern in the simulation results was shown to agree fairly well with the damage pattern in the experimental results. Moreover, it was shown that the prop-rotor blade of a relatively small UAM aircraft can suffer comparatively more damage, even when struck by lightning of the same intensity.

In this study, among three possible lightning strike scenarios for UAM aircraft operating in urban environments, a case was considered in which lightning strikes a UAM aircraft directly. It will be necessary to investigate other remaining cases in the future: (i) when a UAM aircraft is indirectly affected by lightning strikes on other UAM aircraft flying at close range, and (ii) when a nearby high-rise building is struck by lightning and affects adjacent UAM aircraft in flight.

In addition, since batteries, electric motors, inverters, and hydrogen fuel tanks, which are required by the new propulsion systems in UAM aircraft, are being increasingly used, designing a lightning protection system that properly reflects these changes will emerge as an important issue.

Acknowledgments

This work was supported by the National Research Foundation of Korea (NRF) Grant funded by the Ministry of Science, ICT & Future Planning (NRF-2017-R1A5A1015311) and the Korea Institute of Aviation Safety Technology (KIAST) Grant funded by the Ministry of Land, Infrastructure and Transport (21CHTR-C128889-05), South Korea. The authors thank the referees of this paper for valuable and helpful comments and suggestions.

References

[1] Y. Liu, M. Kreimeier, E. Stumpf, Y. Zhou, H. Liu, Overview of recent endeavors on personal aerial vehicle: A focus on the US and Europe research activities, *Progress in Aerospace Sciences*. 91 (2017) 53-66.

[2] U. Eker, G. Fountas, P. Ch. Anastasopoulos, An exploratory empirical analysis of willingness to pay for and use flying cars, *Aerospace Science and Technology.* 104 (2020) 105993.

[3] A. Pukhova, Environmental evaluation of urban air mobility operation, Diss. Master's Thesis, *Technical University of Munich*. Munich, Germany (2018).

[4] A. Straubinger, R. Rothfeld, M. Shamiyeh, K. Buchter, J. Kaiser, K. O. Plotner, An overview of current research and developments in urban air mobility – setting the scene for UAM introduction, *Journal of Air Transport Management*. 87 (2020) 101852.

[5] Y. Zhou, G. Huang, C. Xia, Analysis of fixed-wing VTOL aircraft with gas-driven fan propulsion system, *Aerospace Science and Technology*. 104 (2020) 105984.

[6] T. Lombaerts, J. Kaneshige, M. Feary, Control concepts for simplified vehicle operations of a quadrotor eVTOL vehicle, *AIAA 2020-3189* (2020).

[7] G. Warwick, Getting real: Vehicles are flying, certification regulations and airspace concepts are firming up, and communities are being engaged and educated as urban air mobility moves closer to reality, *Aviation Week & Space Technology*. August 17-20 (2020) 48-53.

[8] G. B. Ahn, K. Y. Jung, R. S. Myong, H. B. Shin, W. G. Habashi, Numerical and experimental investigation of ice accretion on a rotorcraft engine air intake, *Journal of Aircraft*. 52 (3) (2015) 903-909.

[9] L. Prince Raj, L. W. Lee, R. S. Myong, Ice accretion and aerodynamic effects on a multi-element airfoil under SLD icing condition, *Aerospace Science and Technology*. 85 (2019) 320-333.

[10] L. Prince Raj, K. Yee, R. S. Myong, Sensitivity of ice accretion and aerodynamic performance degradation to critical physical and modeling parameters affecting airfoil icing, *Aerospace Science and Technology*. 98 (2020) 105659.

[11] S. Jung, L. P. Raj, A. Rahimi, H. Jeong, R. S. Myong, Performance evaluation of electrothermal anti-icing systems for a rotorcraft engine air intake using a meta model, *Aerospace Science and Technology*. 106 (2020) 106174.

[12] M. D. Patterson, K. R. Antcliff, L. W. Kohlman, A proposed approach to studying urban air mobility missions including an initial exploration of mission requirements, *AHS International 74th Annual Forum & Technology Display* (2018).

[13] M. J. Schuurman, B. Rattanagraikanakorn, R. D. Breuker, C. Kassapoglou, Urban air mobility (UAM) vehicle design considerations to facilitate future accident investigation, *AIAA 2019-3628* (2019).

[14] F. A. Fisher, J. A. Plumer, Lightning protection of aircraft, *NASA LEW-12981* (1977).

[15] B. G. Melander, *Atmospheric Electricity Hazards Threat Environment Definition*, Boeing Military Airplane Co Seattle Wa (1985).

[16] S. H. Han, J. H. Lee, The lightning effects on aircraft and certification, *Journal of the Korean Society for Aeronautical & Space Science*. 31 (9) (2003) 110-120.

[17] F. A. Fisher, J. A. Plumer, Aircraft lightning protection, *NASA AD-A222 716* (1989).

[18] A. Bacchini, E. Cestino, Electric VTOL configurations comparison, *Aerospace*. 6 (3) (2019).

[19] L.A. Lalande, P.B. Clergerie, The lightning swept stroke along an aircraft in flight. Part II: numerical simulations of the complete process, *Journal of Physics D: Applied Physics*. 33 (15) (2000) 1876-1883.

[20] B.S. Lee, A. Tullu, H.Y. Hwang, Optimal design and design parameter sensitivity analyses of an eVTOL PAV in the conceptual design phase, *Applied Sciences*. 10 (15) (2020) 5112.

[21] A. Broc, P. Lalande, E. Montreuil, J. P. Moreau, A. Delannoy, A. Larsson, P. Laroche, A lightning swept stroke model: A valuable tool to investigate the lightning strike to aircraft, *Aerospace Science and Technology*. 10 (8) (2006) 700-708.

[22] F. Moupfouma, Aircraft structure paint thickness and lightning swept stroke damages, *SAE International Journal of Aerospace*. 6 (2) (2013) 392-398.

[23] F. S. Wang, X. S. Yu, S. Q. Jia, P. Li, Experimental and numerical study on residual strength of aircraft carbon/epoxy composite after lightning strike, *Aerospace of Science and Technology*. 75 (2018) 304-314.

[24] J. H. Jo, Y. G. Kim, S. W. Park, R. S. Myong, A study of certification of lightning indirect effects on cable harness in personal air vehicles, *Journal of the Korean Society for Aeronautical & Space Sciences*. 49 (3) (2021) 251-262.

[25] R. Dosoudil, J. Franek, J. Slama, M. Usakova, A. Gruskova, Electromagnetic wave absorption performances of metal alloy/spinel ferrite/polymer composites, *IEEE Transactions on Magnetics*. 48 (4) (2012) 1524-1527.

[26] L. Huang, C. Gao, Lightning indirect effects on helicopter: Numerical simulation and experiment validation, *IEEE Transactions on Electromagnetic Compatibility*. 59 (4) (2017) 1171-1179.

[27] R. Fahdiran, Y. D. Utami, E. Handoko, Effect of different permeability on electromagnetic properties of absorbing materials, *MATECH Web of Conferences*. 197 (2018) 02015.

[28] D. Hentzen, M. Kamgarpour, M. Soler, D. Gonzalez-Arribas, On maximizing safety in stochastic aircraft trajectory planning with uncertain thunderstorm development, *Aerospace Science and Technology*. 79 (2018) 543-553.

[29] D. Gonzalez-Arribas, M. Soler, M. Sanjurjo-Rivo, Robust aircraft trajectory planning under uncertain convective environments with optimal control and rapidly developing thunderstorms, *Aerospace Science and Technology*. 89 (2019) 445-459.

[30] S. W. Park, Y. G. Kim, Y. S. Kang, R. S. Myong, Analysis of effects of lightning on PAV using

Computational simulation and a proposal to establish certification guidance, *Journal of Aerospace System Engineering*. 13 (6) (2019) 60-69.
[31] J.J. Kim, S.T. Beak, D.G. Song, R.S. Myong, Computational simulation of lightning strike on aircraft and design of lightning protection system, Journal of the *Korean Society for Aeronautical and Space Sciences*. 44 (12) (2016) 1071-1086.
[32] Y.G. Kim, H.S. Jo, J.H. Jo, S.W. Park, R.S. Myong, Investigation of effects of lightning and icing on an e-VTOL UAM and a proposal for certification guidance, J. Aerosp. Syst. Eng. 15 (3) (2021) 45-56.
[33] Y. Wang, G. Lu, T. Shi, M. Ma, B. Zhu, D. Liu, C. Peng, Y. Wang, Enhancement of cloud-to-ground lightning activity caused by the urban effect: A case study in the Beijing metropolitan area, *Remote Sensing*. 13 (7) (2021) 1228.
[34] Scott M. Steiger and Richard E. Orville, G. Huffines, Cloud-to-ground lightning characteristics over Houston, Texas: 1989–2000, *Journal of Geophysical Research*. 107 (D11) (2002).
[35] C. M. Rozoff, W. R. Cotton, Simulation of St. Louis, Missouri, Land use impacts on thunderstorms, *Journal of Applied Meteorology*. 42 (2002).
[36] J. A. Stallins, M. L. Bentley, Urban lightning climatology and GIS: An analytical framework from the case study of Atlanta Georgia, *Applied Geography*. 26 (2006) 242-259.
[37] J. A. Stallins, L. S. Rose, Urban lightning: current research, methods, and the geographical perspective, *Geography Compass*. 2 (3) (2008) 620-639.
[38] J. Y. Han, J. J. Baik, A theoretical and numerical study of urban heat island–induced circulation and convection, *Journal of the Atmospheric Sciences*. 65 (6) (2008) 1859-1877.
[39] A. A. Ntelekos, j. A. Smith, L. Donner, J. D. Fast, W. I. Gustafson, J. Elanine, G. Chapman, W. F. Krajewski, The effects of aerosols on intense convective precipitation in the northeastern United States. *Quarterly Journal of the Royal Meteorological Society: A Journal of the Atmospheric Sciences Applied Meteorology and Physical Oceanography*. 135 (643) (2009) 1367-1391.
[40] C. Susan, V. D. Heever, W. R. Cotton, Urban aerosol impacts on downwind convective storms. *Journal of Applied Meteorology and Climatology*. 46 (6) (2007), 828-850.
[41] S. Chang, Ships cause their own stormy seas, *Physics Today*. 70 (11) (2017) 20-21.
[42] *Proposed Means of Compliance with the Special Condition VTOL*, MOC SC-VTOL.
[43] J. B. O'Loughlin, S. R. Skinner, General aviation lightning strike report and protection level study, *Office of Aviation Research, Federal Aviation Administration* (2004).
[44] M. A. Uman, V. A. Rakov, The interaction of lightning with airborne vehicles, *Progress in Aerospace Sciences*. 39 (2003) 61-81.
[45] FSF Editorial Staff, Helicopter downed in North Sea after lightning strike exceeds lightning-protection system capabilities, *Flight Safety Foundation Helicopter Safety*. 24 (1) (1998).
[46] J. J. Barnett, Report on the accident to Sikorsky S-76A+, G-BJVX near the leman 49/26 foxtrot platform in the North Sea 16 July 2002, *The United Kingdom for the Air Accidents Investigation Branch,* (2005).
[47] K. Nakahashi, T. Miyashita, T. Ishikawa, S. Tamura, K. Tanaka, M. Nakanishi, Aircraft accident investigation report, *The Japan Transport Safety Board* (2016).
[48] D. Cade, *This Is What Happens When a Drone Is Struck by Lightning* (2017).
[49] Aircraft lightning zone, *SAE ARP5414B*.
[50] O. Spiller, *Electromagnetic Effects Harmonization Working Group (EEHWG)-Lightning Task Group: Report on Aircraft Lightning Strike Data*, United States Federal Aviation Administration (2002).
[51] V. Mazur, A physical model of lightning initiation on aircraft in thunderstorms, *Journal of*

Geophysical Research. 94 (D3) (1989) 3326-3340.
[52] P. Lalande, A. B. Clergerie, P. Laroche, Computations of the initial discharge initiation zones on aircraft or helicopter, *SAE Technical Paper 1999-01-2371* (1999).
[53] A. Larsson, The interaction between a lightning flash and an aircraft in flight, *Comptes Rendus Physique*. 3 (10) (2002) 1423-1444.
[54] A. Broc, A. Delannoy, E. Montreuil, P. Lalande, P. Laroche, Lightning strike to helicopters during winter thunderstorms over North Sea, *Aerospace Science and Technology*. 9 (8) (2005) 686-691.
[55] M. Apra, M. D'Amore, K. Gigliotti, M. S. Sarto, V. Volpi, Lightning indirect effects certification of a transport aircraft by numerical simulation, *IEEE Transactions on Electromagnetic Compatibility*. 50 (3) (2008) 513-523.
[56] T. Zou, J. Wang, K. Mao, Z. Feng, Simulation of lightning protection for composite civil aircraft, *Procedia Engineering*. 17 (2011) 328-334.
[57] P. Lalande, A. Delannoy, Numerical methods for zoning computation, *AerospaceLab*. 5 (2012) 1-10.
[58] M. Kunze, *Simulating Lightning Attachment and Strikes on Aircraft Whitepaper* (2018).
[59] A.R. Gnadt, S. Isaacs, R. Price, M. Dethy, C. Chappelle, Hybrid turbo-electric STOL aircraft for urban air mobility, *AIAA 2019-0531* (2019).
[60] S. Addarkaoui, A. Bernier, Y. Chen, H. Compere, A. Dore, M. Fransolet, R. Jumpertz, L. Macchialolo, Graduate team aircraft design competition: electric vertical takeoff and landing(E-VTOL) aircraft mistral air taxi, *AIAA Graduate Team Aircraft Design Competition 2018-2019* (2019).
[61] Y. Karamian, S.R. Fattahi, F. Rassouli, S. Mohammad, H. Akbari, M. Ghasemi, A. Akbari, M. R. Najafi, M. Alizadeh, M. H. Sabeti, Z Saedi, M. M. Mohnmmadi, An on-demand energy-efficient E-VTOL airtaxi, *AIAA Graduate Team Aircraft Design Competition 2018-2019* (2019).
[62] B. Passe, J. Baeder, *Computational Aeroacoustics of Various Propeller Designs for eVTOL Applications*, Doctoral Dissertation, University of Maryland, Baltimore, 2019
[63] L. Koers, *Modelling of a Ducted Fan and its Contribution to Drag on a PAV Hull*, Master's Thesis, University of Twente, Drienerlolaan, 2019.
[64] Y.T. Kim, C.H. Park, H.Y. Kim, Performance analysis of coaxial propeller for multicopter type PAV (Personal Air Vehicle), *Journal of Aerospace System Engineering*. 13 (3) (2019) 56-63.
[65] H. Lee, D.J. Lee, Rotor interactional effects on aerodynamic and noise characteristics of a small multirotor unmanned aerial vehicle, *Physics of Fluids*. 32 (4) (2019) 047107.
[66] M. Skuhersky, *A First-principle Power and Energy Model for eVTOL Vehicles*, Doctoral Dissertation, Florida Institute of Technology, Melbourne, 2019.
[67] W.G. Bousman, *Airfoil Dynamic Stall and Rotorcraft Maneuverability*, NASA Ames Research Center, Moffett Field, California, 2000.
[68] W. Kania, W. Stalewski, B. Zwierzchowska, *Design of the Modern Family of Helicopter Airfoils*, Prace Instytutu Lotnictwa. (2007) 51-82.
[69] B. Rasuo, Helicopter tail rotor blade from composite materials: an experience, SAE *International Journal of Aerospace*. 4 (2011-01-2545) (2011) 828-838.
[70] D. Garinis, M. Dinulovic, B. Rasuo, Dynamic analysis of modified composite helicopter blade, *FME Transactions*. 40 (2) (2012) 63-68.
[71] I. Tawk, J. Aubry, P. Navarro, J.F. Ferrero, S. Marguet, S. Rivallant, S. Lemaire, P. Rauch, Study of impact on helicopter blade, *Engineering Failure Analysis*. 24 (2012) 38-45.
[72] N. A. Vu, J. W. Lee, J. I. Shu, Aerodynamic design optimization of helicopter rotor blades including airfoil shape for hover performance, *Chinese Journal of Aeronautics*. 26 (1) (2013) 1-8.

[73] M. Amura, L. Aiello, M. Colavita, F.D. Paolis, M. Bernabei, Failure of a helicopter main rotor blade, *Procedia Materials Science*. 3 (2014) 726-731.

[74] M.S. Gupta, B.U. Kumar, Design and analysis of Black Hawk UH-60 rotor blade using composite materials, *International Journal & Magazine of Engineering*. 3 (9) (2016) 755-763.

[75] N. Mohd, G. Barakos, Performance and wake analysis of rotors in axial flight using computational fluid dynamics, *Journal of Aerospace Technology and Management*. 9 (2) (2017) 193-202.

[76] R.M. Eshcol, Y. Dewan, Numerical design optimization of the S-76 rotor for hover performance, *2018 AIAA Aerospace Sciences Meeting* (2018).

[77] W.Y. Pas, S. Haldar, C.V. Singh, Performance analysis of composite helicopter blade using synergistic damage mechanics approach, *AIAA Journal*. 58 (2) (2020) 968-976.

[78] S. P. Scroger, J. Palaclos, Empirical modeling of urban air mobility rotor icing thrust degradation, *AIAA 2020-2816* (2020).

[79] J. Jeong, H. Shi, K. Lee, B. Kang, Improvement of electric propulsion system model for performance analysis of large-size multicopter UAVs, *Applied Sciences*. 10 (22) (2020) 8080.

[80] A. Jain, K. Bavikar, A. Sanjay, Baseline procedure for conceptual designing of an eVTOL for urban air mobility, *In 2020 4th International Conference on Electronics, Communication and Aerospace Technology*. (2020) 1173-1178.

[81] S. Suesse, M. Hajek, Rotor blade displacement and load estimation with fiber-optical sensors for a future health and usage monitoring system, *Conference AHS 74th Annual Forum, At Phoenix, AZ, USA* (2018).

[82] B. Alemour, O. Badran, M. R. Hassan, A review of using conductive composite materials in solving lightning strike and ice accumulation problems in aviation, *Journal of Aerospace Technology and Management*. 11 (2019).

[83] Y. Wang, T. K. Risch, J. H. Koo, Assessment of a one-dimensional finite element charring ablation material response model for phenolic-impregnated carbon ablator, *Aerospace Science and Technology*. 91 (2019) 301-309.

[84] J. H. Boelens, *Pioneering the Urban Air Taxi Revolution* (White Paper) (2019).

[85] E. Xu, *The Future of Transportation: White Paper on Urban Air Mobility Systems* (White Paper) (2020).

[86] *Mobility Technology Unfolds Skywards*, Hyundai Motor Group, 2021.

[87] T. Ogasawara, Y. Hirano, A. Yoshimura, Coupled thermal-electrical analysis for carbon fiber/epoxy composites exposed to simulated lightning current, *Composites Part A: Applied Science and Manufacturing*. 41 (8) (2010) 973-981.

[88] L. Chemartin, P. Lalande, B. Peyrou, A. Chazottes, P. Q. Elias, C. Delalondre, B. G. Cheron, F. Lago, Direct effects of lightning on aircraft structure: Analysis of the thermal, electrical and mechanical constraints, *AerospaceLab*. 5 (2012) 1-15.

[89] R. Ranjith, R. S. Myong, Computational investigation of lightning strike effects on aircraft components, *International Journal of Aeronautical and Space Sciences*. 15 (1) (2014) 44-53.

[90] G. Abdelal, A. Murphy, Nonlinear numerical modelling of lightning strike effect on composite panels with temperature dependent material properties, *Composite Structures*. 109 (2014) 268-278.

[91] Y. S. Kang, S. W. Park, J. S. Roh, R. S. Myong, Computational investigation of effects of expanded metal foils on the lightning protection performance of a composite rotor blade, *International Journal of Aeronautical and Space Sciences*. 22 (2021) 203-221.

[92] H. Kawakami, P. Feraboli, Lightning strike damage resistance and tolerance of scarf-repaired mesh-protected carbon fiber composites, *Composites Part A: Applied Science and Manufacturing*.

42 (9) (2011) 1247-1262.
[93] F. S. Wang, Y. Zhang, X. T. Ma, Z. Wei, J. F. Gao, Lightning ablation suppression of aircraft carbon/epoxy composite laminates by metal mesh, *Journal of Materials Science & Technology*. 35 (11) (2019) 2693-2704.
[94] J. Morgan, Thermal simulation and testing of expanded metal foils used for lightning protection of composite aircraft structures, *SAE International Journal of Aerospace*. 6 (2) (2013) 371-377.
[95] M. Gagne, D. Therriault, Lightning strike protection of composites, *Progress in Aerospace Science*. 64 (2014) 1-16.
[96] X. Ma, F. Scarpa, H. X. Peng, G. Allegri, J. Yuan, R. Ciobanu, Design of a hybrid carbon fibre/carbon nanotube composite for enhanced lightning strike resistance, *Aerospace Science and Technology*. 47 (2015) 367-377.
[97] A. Katunin, K. Krukiewicz, A. Herega, G. Catalanotti, Concept of a conducting composite material for lightning strike protection, *Advances in Materials Science*. 16 (2) (2016) 32-46.
[98] Y. Guo, Y. Xu, Q. Wang, Q. Dong, X. Yi, Y. Jia, Enhanced lightning strike protection of carbon fiber composites using expanded foils with anisotropic electrical conductivity, *Composites Part A: Applied Science and Manufacturing*. 117 (2019) 211-218.
[99] Aircraft lightning environment and related test waveforms, *SAE ARP5412B*.
[100] P. Feraboli, M. Miller, Damage resistance and tolerance of carbon/epoxy composite coupons subjected to simulated lightning strike, *Composites: Part A*. 40 (2009) 954-967.
[101] S. I. Braginskii, Theory of the development of a spark channel, *Sov. Phys. JETP*. 34 (7) (1958) 1068-1074.
[102] M. N. Plooster, Numerical model of the return stroke of the lightning discharge, *The Physics of Fluids*. 14 (10) (1971) 2124-2133.
[103] R. D. Hill, Channel heating in return-stroke lightning, *Journal of Geophysical Research*. 76 (3) (1971) 637-645.
[104] A. H. Paxton, R. L. Gardner, L. Baker, Lightning return stroke. a numerical calculation of the optical radiation, *The Physics of Fluids*. 29 (8) (1986) 2736-2741.
[105] R. D. Hill, Lightning channel decay, *Physics of Fluids B: Plasma Physics*. 2 (12) (1990) 3209-3211.
[106] M. Tanaka, K. Yamamoto, S. Tashiro, K. Nakata, E. Yamamoto, K. Yamazaki, K. Suzuki, A. B. Murphy, J. J. Lowke, Time-dependent calculations of molten pool formation and thermal plasma with metal vapour in gas tungsten arc welding, *Journal of Physics D: Applied Physics*. 43 (43) (2010) 434009.
[107] C. Perera, M. Rahman, M. Fernando, P. Liyanage, V. Cooray, The relationship between current and channel diameter of 30 cm long laboratory sparks, *Journal of Electrostatics*. 70 (6) (2012) 512-516.
[108] Y. Wang, O. I. Zhupanska, Lightning strike thermal damage model for glass fiber reinforced polymer matrix composites and its application to wind turbine blades, *Composite Structures*. 132 (2015) 1182-1191.
[109] Y. Wang, O. I. Zhupanska, Modeling of thermal response and ablation in laminated glass fiber reinforced polymer matrix composites due to lightning, *Applied Mathematical Modelling*. 53 (2018) 118-131.
[110] J. H. Lee, T. E. Lacy Jr, C. U. Pittman Jr, M. S. Mazzola, Thermal response of carbon fiber epoxy laminates with metallic and nonmetallic protection layers to simulated lightning currents, *Polymer Composites*. 39 (S4) (2018) E2149-E2166.
[111] Q. Dong, G. Wan, Y. Guo, L. Zhang, X. Wei, X. Yi, Y. Jia, Damage analysis of carbon fiber

composites exposed to combined lightning current components D and C, *Composites Science and Technology*. 179 (2019) 1-9.
[112] M. Long, *On the Attachment of Lightning Flashes to Wind Turbines*, KTH Royal Institute of Technology (2016).
[113] F. Bouchut, On the discrete conservation of the Gauss-Poisson equation of plasma physics, *Communications in Numerical Methods in Engineering*. 14 (1) (1998) 23-34.
[114] S. Yidirim, Exact and numerical solution of Poisson equation for electrostatic potential problems, *Mathematical Problem in Engineering*. 2008 (2008) 1-11.
[115] J.R. Nagel, Solving the generalized Poisson equation using the finite-difference method (FDM), *IEEE Antennas and Propagation Magazine*. 56 (2012) 524-550.
[116] C. Su, H. Ke, T. Hubing, Overview of electromagnetic modeling software, *Proc. of the 25th International Review of Progress in Applied Computational Electromagnetics*. (2009) 736-741.
[117] K.S. Yee, Numerical solution of initial boundary value problems involving maxwell's equation in isotropic media, *IEEE Transactions on Antennas and Propagation*. 14 (3) (1966) 302-307.
[118] J. Fisher, P.R. Hoole, K. Pirapaharan, S. H. Hoole, Pre-lightning strikes and aircraft electrostatics, *EDP Sciences*. 87 (2017).
[119] M. Kunze, Efficient assessment of aircraft initial lightning attachment zones based on electrostatic simulations, *Proceedings of International Conference on Lightning and Static Electricity, Nagoya*, Japan. 2017.
[120] *Advisory Circular 27-1B*, U.S. Department of Transportation Federal Aviation Administration, 2014.
[121] *Advisory Circular 29-2C*, U.S. Department of Transportation Federal Aviation Administration, 2014.
[122] Akrilik Kimya Sanayii AS, 3K A-38 Technical Data Sheet, Dowaksa Carbon Fiber, Turkey, 2013.
[123] Akrilik Kimya Sanayii AS, *6K A-38 Technical Data Sheet*, Dowaksa carbon fiber, Turkey, 2012.
[124] T. Hu, X. Yu, Lightning performance of copper-mesh clad composite panels: Test and simulation, Coatings. 9 (11) (2019) 727.
[125] R. Munoz, S. Delgado, C. Gonzalez, B. Lopez-Romano, D. Y. Wang, J. LLorca, Modeling lightning impact thermo-mechanical damage on composite materials, *Applied Composite Materials*. 21 (1) (2014) 149-164.
[126] K. Yousefpour, W. Lin, Y. Wang, C. Park, Discharge and ground electrode design considerations for the lightning strike damage tolerance assessment of CFRP matrix composite laminates, *Composites Part B: Engineering*. 198 (2020).
[127] Y. Hirano, S. Katsumata, Y. Iwahori, A. Todoroki, Artificial lightning testing on graphite/epoxy composite laminate, *Composites Part A: Applied Science and Manufacturing*. 41 (10) (2010) 1461-1470.
[128] G. W. Jeong, Y. H. Noh, W. H. Choi, J. H. Shin, J. H. Kweon, J. G. Yook, Y. W. Nam, Electromagnetic-mechanical repair patch of radar-absorbing structure with electroless nickel-plated glass fabric damaged by lightning strike, *Journal of Composite Materials*. 55 (7) (2021) 989-1002.
[129] J. Chen, X. Bi, J. Liu, Z. Fu, Damage investigation of carbon-fiber-reinforced plastic laminates with fasteners subjected to lightning current component C and D, *Applied Sciences*. 10 (6) (2020) 2147.
[130] A. Duongthipthewa, M. Lu, K. Du, L. Ye, L. Zhou, Experimental and numerical simulation of lightning damage development on composites with/without a carbon-based protection layer, *Composite Structures*. 260 (2021).

[131] L. Chemartin, P. Lalande, C. Delalondre, B. Cheron, F. Lago, Modelling and simulation of unsteady dc electric arcs and their interactions with electrodes, *Journal of Physics D: Applied Physics*. 44 (19) (2011).

[132] *Composite Materials Handbook*, MIL-HDBK-17-2F Volume 2 of 5 (2002).

[133] Y. Wang, *Modeling of Lightning-induced Thermal Ablation Damage in Anisotropic Composite Materials and its Application to Wind Turbine Blades*, University of Iowa (2016)

[134] *Heat Transfer Module User's Guide 2020*, COMSOL.

[135] *COMSOL Multiphysics Reference Manual 2019*, COMSOL.